A NEAR-INFRARED SPECTROSCOPIC STUDY OF YOUNG FIELD ULTRACOOL DWARFS

K. N. Allers[1,3] and Michael C. Liu[2,3]

[1] Department of Physics and Astronomy, Bucknell University, Lewisburg, PA 17837, USA; k.allers@bucknell.edu
[2] Institute for Astronomy, University of Hawaii, 2680 Woodlawn Drive, Honolulu, HI 96822, USA

ABSTRACT

We present a near-infrared (0.9–2.4 μm) spectroscopic study of 73 field ultracool dwarfs having spectroscopic and/or kinematic evidence of youth ($\approx$10–300 Myr). Our sample is composed of 48 low-resolution ($R \approx 100$) spectra and 41 moderate-resolution spectra ($R \gtrsim 750$–2000). First, we establish a method for spectral typing M5–L7 dwarfs at near-IR wavelengths that is independent of gravity. We find that both visual and index-based classification in the near-IR provides consistent spectral types with optical spectral types, though with a small systematic offset in the case of visual classification at J and K band. Second, we examine features in the spectra of $\sim$10 Myr ultracool dwarfs to define a set of gravity-sensitive indices based on FeH, VO, K I, Na I, and H-band continuum shape. We then create an index-based method for classifying the gravities of M6–L5 dwarfs that provides consistent results with gravity classifications from optical spectroscopy. Our index-based classification can distinguish between young and dusty objects. Guided by the resulting classifications, we propose a set of low-gravity spectral standards for the near-IR. Finally, we estimate the ages corresponding to our gravity classifications.

Key words: brown dwarfs – infrared: stars – planets and satellites: atmospheres – stars: low-mass

Online-only material: color figures

1. INTRODUCTION

Brown dwarfs occupy the mass range between stars and planets. Because they are not massive enough to sustain hydrogen burning in their cores, they continually cool over their lifetimes. In addition, brown dwarfs contract as they age, evolving from low to high surface gravity. Thus, brown dwarfs do not occupy a main sequence, and the spectral type of a brown dwarf cannot provide a unique determination of its mass.

The dividing line between brown dwarfs and exoplanets is customarily taken to be the minimum mass at which an object fuses deuterium (11.4–14.4 $M_{\rm Jupiter}$; Spiegel et al. 2011). This mass boundary does not discriminate between the possible origins of the object. Is NGC 4349 127 b, a 20 $M_{\rm Jup}$ radial velocity companion (Lovis & Mayor 2007) to an intermediate-mass star (3.9 $M_\odot$), best characterized as a brown dwarf? Should Cha 110913-773444, an 8 $M_{\rm Jup}$ free-floating object with a circumstellar disk (Luhman et al. 2005), be considered a planet? The dividing line between planets and brown dwarfs has been further blurred by the discovery of directly imaged exoplanets (Marois et al. 2008; Lagrange et al. 2009). In particular, the HR 8799 planets have very red near-IR colors, similar to the reddest known field L-type brown dwarfs. The remarkably red colors of some L dwarfs have been attributed to youth (Kirkpatrick et al. 2008; Barman et al. 2011) and/or an unusually dusty photosphere (McLean et al. 2003; Cushing et al. 2005; Looper et al. 2008). It is interesting to note that spectroscopy and photometry of the HR 8799 planets are best matched by young, dusty atmospheres (e.g., Bowler et al. 2010; Madhusudhan et al. 2011; Barman et al. 2011). Thus, better understanding of the properties of young and/or dusty field brown dwarfs may provide important insights on the atmospheres of directly imaged exoplanets.

A number of field brown dwarfs having spectroscopic indicators of youth have been reported (e.g., Reid et al. 2008; Cruz et al. 2004). To date, these studies have mainly focused on the optical spectroscopic properties of low-gravity M and L field dwarfs (Cruz et al. 2009; Kirkpatrick et al. 2008). Only a handful of young field brown dwarfs have been studied in detail in the near-infrared (e.g., Allers et al. 2010; Kirkpatrick et al. 2006). There are a number of reasons to study young field brown dwarfs in the infrared. First, the spectral energy distributions (SEDs) of late-M and L dwarfs peak in the near-infrared, making them easiest to study at these wavelengths. Second, studies of directly imaged exoplanets have been conducted in the near-IR, where the planet-to-star flux ratio is most favorable and ground-based adaptive optics systems have the best performance. Thus, direct spectroscopic and photometric comparison of exoplanets and brown dwarfs is feasible in the near-IR (e.g., Bowler et al. 2010). Finally, the near-IR spectra of the youngest brown dwarfs contain a wealth of gravity-sensitive features (Allers et al. 2007).

In this paper, we present the largest near-IR spectroscopic sample to date of young ($\lesssim$200 Myr old) field ultracool dwarfs. Our sample consists of 73 late-M and L-type dwarfs displaying spectral signatures of youth and/or kinematic evidence for membership in a young moving group. At young ages ($\lesssim$125 Myr old), objects with spectral types later than M6.5 are below the hydrogen burning mass limit (Stauffer et al. 1998). Thus, the vast majority of our sample is comprised of brown dwarfs. In this work, we determine near-IR spectral types and examine gravity (age) sensitive features in low and moderate resolution near-IR spectra of young field brown dwarfs. We develop a set of indices to classify the gravity of these objects and create a gravity classification system for use in the near-IR that provides results consistent with gravity classifications from optical spectroscopy (Cruz et al. 2009). We then compare our findings on young field objects to objects with well-determined ages.

2. OUR SAMPLE

Our sample consists of 89 spectra for 73 M5–L7 objects that have published spectroscopic or kinematic evidence of youth (see Table 1 and references therein). Thirty of our spectra are for objects having gravity determinations from

---

Table 1
Near-IR Spectral Types

Object	SpT	References			SpT (Visual)		SpT (Index)				SpT
	Optical	Opt. SpT	Youth	NIR Spec.	J-band[a]	K-band[a]	H_2O	H_2OD	H_2O-1	H_2O-2	Final
					Low-resolution near-IR spectra						
2MASS J00274197+0503417[b]	M9.5	K95	K95, M99	A13	L0.0	L0.0	M9.0 ± 0.6	M7.0 ± 1.0	L0.5 ± 1.1	M9.3 ± 0.7	L0
2MASS J00325584−4405058	L0.0γ	R08, C09	C09	A13	L1.5	L0.0	M9.9 ± 0.6	M9.8 ± 0.8	L0.0 ± 1.1	M9.3 ± 0.6	L0
2MASS J00332386−1521309	L4.0β	R08, C09	C09	A13	L1.5	L1.0	L0.4 ± 0.5	L1.9 ± 0.8	M8.6 ± 1.1	L0.6 ± 0.6	L1
WISEP J004701.06+680352.1	···	···	G12	G12	L8.0:	L6.0:	···	L6.2 ± 0.8	···	···	L7
2MASS J01033203+1935361	L6.0β	K00, F12	F12	C04	L7.0	L6.0	···	L5.2 ± 0.8	···	···	L6
2MASS J01174748−3403258	L2.0	C03	F09	B08	L3.0	L2.0	L0.8 ± 0.6	L1.5 ± 0.8	M9.9 ± 1.1	L1.6 ± 0.6	L1
2MASS J01262109+1428057	L4.0γ	F13	M08	M08	L6.0:	L1.5	L2.7 ± 1.2	L2.5 ± 0.9	L0.1 ± 1.3	M8.8 ± 0.8	L2
2MASS J01415823−4633574	L0.0γ	C09, K06	K06	K06	L2.0	L0.0	M9.7 ± 0.5	M8.7 ± 0.8	L0.1 ± 1.1	M9.4 ± 0.5	L0
2MASS J02292794−0053282	···	···	G11	A13	L2.0	L0.5	M9.7 ± 1.3	M9.5 ± 1.2	L0.3 ± 1.2	M9.7 ± 1.1	L0
2MASS J02411151−0326587	L0.0γ	C09	C09	A13	L2.0	L0.0	L2.3 ± 0.9	M9.9 ± 0.9	L1.4 ± 1.2	L0.4 ± 0.8	L1
2MASS J03350208+2342356	M8.5	R02	S09	A13	M7.5	M7.0	M7.2 ± 0.4	···	M7.8 ± 1.1	M7.0 ± 0.5	M7
LP 944−20	M9.0	C03	T98, R09	B08	L0.0	L0.0	M9.1 ± 0.4	M9.1 ± 0.8	L0.3 ± 1.1	M9.3 ± 0.5	L0
2MASS J03552337+1133437	L5.0γ	C09	C09	F13	L6.5:	L1.0:	L2.8 ± 0.6	L2.6 ± 0.8	M9.0 ± 1.2	···	L3
2MASS J04062677−3812102	L0.0γ	K10	K10	K10	L2.0:	L1.0	L1.7 ± 1.6	L1.7 ± 1.2	M7.5 ± 1.4	M9.2 ± 1.3	L1
2MASS J04070752+1546457	L3.5	R08	R08	A13	L3.5	L3.0	L3.4 ± 0.4	L3.8 ± 0.8	L1.6 ± 1.1	···	L3
2MASS J05012406−0010452	L4.0γ	R08, C09	C09	A10	L5.0:	L2.5:	L2.9 ± 0.5	L1.8 ± 0.8	L1.7 ± 1.1	···	L3
2MASS J05184616−2756457	L1.0γ	F13	F13	A13	L3.0	L1.5	L1.7 ± 0.6	L0.2 ± 0.9	L0.1 ± 1.1	L1.3 ± 0.6	L1
2MASS J05341594−0631397	M8.0γ	K10	K10	K10	M7.5	M8.0	M7.9 ± 1.0	···	M9.2 ± 1.2	M6.6 ± 1.1	M8
2MASS J05361998−1920396	L2.0γ	F13	F13	A13	L3.0:	L2.5	L2.4 ± 0.7	L1.4 ± 0.8	L2.1 ± 1.1	L1.2 ± 0.6	L2
2MASS J05575096−1359503	M7.0	C07	S09	A13	M8.0	M6.5	M6.9 ± 0.4	···	M6.9 ± 1.1	M6.6 ± 0.5	M7
2MASS J06085283−2753583	M9.0γ	C03, R10	R10	A13	L0.0	L0.0	M9.5 ± 0.5	M9.2 ± 0.8	L0.3 ± 1.1	M9.7 ± 0.6	L0
2MASS J06195260−2903592	M6.0	C03	C03	A13	···	M6.5	M6.0 ± 0.9	···	M2.9 ± 1.3	M5.7 ± 0.8	M5
G 196−3B	L3.0	C09	R98, K01	A10	L5.0:	L2.0	L3.4 ± 0.5	L2.6 ± 0.8	L3.6 ± 1.1	···	L3
SDSS J102552.43+321234.0	···	···	K08	C06	L7.5	L6.5	···	L6.3 ± 0.8	···	···	L7
DENIS-P J104731.1−181558	L2.5	M99	S10	A13	L0.5	L1.0	L0.2 ± 0.6	L1.5 ± 0.8	M8.6 ± 1.1	L0.2 ± 0.7	L0
Gl 417B	L4.5	K08	K01, K08	B10	L5.5	L4.5:	···	L4.8 ± 0.8	L3.2 ± 1.1	···	L5
TWA 26 (2M J1139−31)	M9.0	R08	G02	L07	L0.0:	M9.0	M9.1 ± 0.4	···	M9.8 ± 1.1	M8.6 ± 0.5	M9
TWA 27A (2M J1207−39A)	M8.0	G02	G02	L07	M8.0	M8.0	M7.9 ± 0.4	···	M9.2 ± 1.1	M7.4 ± 0.5	M8
TWA 27B (2M J1207−39B)	···	···	Ch04	P12	L5.0:	L3.0:	L0.2 ± 0.4	···	···	···	L3
TWA 29 (2M J1245−44)	M9.5	L07	L07, W13	L07	L0.5	L0.0	M9.4 ± 0.7	M9.1 ± 0.9	M9.6 ± 1.1	M8.9 ± 0.8	L0
2MASS J15474719−2423493	M9.0	R08	R08, K08	A13	L0.0	L0.0	M8.9 ± 0.5	M9.2 ± 0.8	M9.6 ± 1.1	M9.2 ± 0.6	L0
2MASS J15515237+0941148	L4.0γ	F13	R08	A13	L5.0	L3.5:	L4.6 ± 1.3	L3.4 ± 0.9	L3.2 ± 1.2	···	L4
2MASS J15525906+2948485	L0.0β	C09	C09	A13	L1.5	L0.0	L0.6 ± 0.4	M9.7 ± 0.8	L0.2 ± 1.1	M9.9 ± 0.5	L0
2MASS J15575011−2952431	M9.0δ	K10	K10	K10	L0.0	L2.0:	M9.6 ± 1.5	L0.8 ± 1.4	L2.3 ± 1.2	L1.4 ± 1.4	L1
2MASS J16154255+4953211	L4.0γ	F13	C07, K08	A13	L6.0:	L3.0	L3.4 ± 0.6	L3.0 ± 0.8	L1.7 ± 1.1	···	L3
2MASS J17054834−0516462	L0.5	R08	S10	B10	L1.0	L1.0	L1.2 ± 0.4	L1.2 ± 0.8	L0.8 ± 1.1	L0.7 ± 0.5	L1
2MASS J17073334+4301304	L0.5	C03	C03	A13	L0.0	L0.0	M8.6 ± 0.5	···	M8.7 ± 1.1	M9.5 ± 0.6	M9
2MASS J17111353+2326333	L0.0	C07	W08	A13	L0.0	L0.5	L1.8 ± 1.0	L0.1 ± 1.1	L1.9 ± 1.2	L0.4 ± 0.9	L1
2MASS J17260007+1538190	L3.0β	C09	C09	A13	L4.5:	L2.0	L3.1 ± 0.7	L2.9 ± 0.8	L2.5 ± 1.1	···	L3
2MASS J17312974+2721233	L0.0	R08	S10	A13	L0.5	L0.0	M9.0 ± 0.4	M9.5 ± 0.8	M8.9 ± 1.1	M8.9 ± 0.5	L0
2MASS J19355595−2846343	M9.0	R08	M10	A13	L0.5	L0.0	M9.0 ± 0.4	···	M8.6 ± 1.1	M8.8 ± 0.5	M9
2MASS J20135152−2806020	M9.0	R08	R08	A13	L0.5	L1.0	L0.0 ± 0.4	M8.9 ± 0.8	M9.7 ± 1.1	M9.9 ± 0.5	L0
2MASS J20575409−0252302	L1.5	C03	C03, S10	B08	L1.5	L2.5:	L1.3 ± 0.5	L2.1 ± 0.8	L1.4 ± 1.1	L1.1 ± 0.5	L2
DENIS-P J220002.0−303832	L0.0	R08	S10	B06	M9.0	M8.0	M8.5 ± 0.5	···	M7.8 ± 1.1	M9.0 ± 0.6	M9
2MASS J22081363+2921215	L3.0γ	C09	C09	A13	L4.0	L2.0	L2.7 ± 0.7	L2.1 ± 0.8	L2.4 ± 1.1	···	L3
2MASS J22134491−2136079	L0.0γ	C09	C09	A13	L2.0	L0.0	L0.4 ± 0.5	L0.0 ± 0.8	M8.4 ± 1.1	M9.5 ± 0.6	L0
2MASS J22443167+2043433	L6.5	K08	K08	L08	L7.5	L5.0:	···	L6.1 ± 0.8	···	···	L6
SDSS J224953.47+004404.6AB	L3.0	H02	A10	A10	L5.0	L3.0	L3.3 ± 0.5	L3.1 ± 0.8	L2.5 ± 1.1	···	L3
					Moderate-resolution near-IR spectra						
2MASS J00034227−2822410	M7.5	C07	S09	A13	M8.0	M7.0	M7.3 ± 0.4	···	M6.3 ± 1.1	M7.5 ± 0.5	M7
2MASS J00192626+4614078	M8.0	C03	R09	A13	M7.0	M8.0	M7.5 ± 0.4	···	M8.2 ± 1.1	M7.7 ± 0.5	M8
2MASS J00452143+1634446	L2.0β	C09	C09	A13	L2.0	L2.0	L1.7 ± 0.4	L1.1 ± 0.8	L2.4 ± 1.1	L1.3 ± 0.5	L2
2MASS J01033203+1935361	L6.0β	K00, F12	F12	M03	L6.5:	L6.0	···	L5.9 ± 0.8	···	···	L6
SERC 296A	M6.0	T97	T97	A13	M5.5	M6.0	M5.5 ± 0.4	···	M6.5 ± 1.1	M5.5 ± 0.5	M6
2MASS J01415823−4633574	L0.0γ	C09, K06	K06	K06	L2.0	L1.0	L0.2 ± 0.4	M7.2 ± 0.8	L0.4 ± 1.1	M9.1 ± 0.5	L0
GSC 08047−00232B	···	···	Ch05a	P12	L1.0:	L1.0	L0.9 ± 0.4	L0.9 ± 0.8	L3.5 ± 1.1	L0.5 ± 0.5	L1
2MASSI J0253597+320637	M7.5	C03	C03	A13	M6.0	M6.0	M5.8 ± 0.4	···	M5.2 ± 1.1	M5.6 ± 0.5	M6
2MASS J03140344+1603056	L0.0	R08	S10	A13	M8.5	L0.0	M9.8 ± 0.4	M9.6 ± 0.8	L0.1 ± 1.1	M9.4 ± 0.5	L0
2MASS J03350208+2342356	M8.5	R02	S09	A13	M7.0	M7.0	M7.2 ± 0.4	···	M8.6 ± 1.1	M7.2 ± 0.5	M7
LP 944−20	M9.0	C03	T98, R09	A13	L1.0	L0.0	M9.7 ± 0.4	M9.0 ± 0.8	L0.8 ± 1.1	M9.6 ± 0.5	L0
2MASS J03552337+1133437	L5.0γ	C09	C09	A13	L7.0:	L2.0	L2.1 ± 0.4	L3.0 ± 0.8	L1.2 ± 1.1	···	L3
2MASS J04221413+1530525	M6.0γ	R08	R08	A13	···	M6.5	M7.2 ± 0.4	···	M5.5 ± 1.1	M5.9 ± 0.5	M6

Table 1
(Continued)

Object	SpT Optical	References			SpT (Visual)		SpT (Index)				SpT Final
		Opt. SpT	Youth	NIR Spec.	J-band[a]	K-band[a]	H_2O	H_2OD	H_2O-1	H_2O-2	
2MASS J04351455−1414468	M7.0	C03	C03	A13	⋯	M8.0	M8.4 ± 0.4	⋯	M5.8 ± 1.1	M7.4 ± 0.5	M7
2MASS J04362788−4114465	M8.0	C07	C07	A13	M8.0	M9.0	M8.4 ± 0.4	⋯	M9.7 ± 1.1	M8.5 ± 0.5	M9
2MASS J04433761+0002051	M9.5	C07	R09, M10	A13	L0.0	L0.0	M9.3 ± 0.4	M8.1 ± 0.8	L1.1 ± 1.1	M9.6 ± 0.5	L0
2MASS J05575096−1359503	M7.0	C07	S09	A13	M8.0	M7.0	M7.1 ± 0.4	⋯	M7.0 ± 1.1	M6.6 ± 0.5	M7
2MASS J06023045+3910592	L1.0	S03	S03, S10	A13	L2.0	L1.5	L2.0 ± 0.4	L1.4 ± 0.8	L2.1 ± 1.1	L1.1 ± 0.5	L2
2MASS J06085283−2753583	M9.0γ	C03, R10	R10	R10	L1.5	L0.5	L0.6 ± 0.4	M8.4 ± 0.8	L1.2 ± 1.1	L0.0 ± 0.5	L0
CD−35 2722B	⋯	⋯	W11	W11	L4.0:	L3.0:	L2.5 ± 0.4	⋯	L3.1 ± 1.1	⋯	L3
AB PicB	⋯	⋯	Ch05b	P12	L0.5	L0.0	M9.5 ± 0.4	M8.5 ± 0.8	L2.9 ± 1.1	M9.2 ± 0.5	L0
LP 423−31	M7.0	C03	C03, S09	A13	M6.5	M6.0	M5.7 ± 0.4	⋯	M5.4 ± 1.1	M5.9 ± 0.5	M6
2MASS J08040580+6153336	M9.0	R08	S07	A13	M9.0	M7.0	M8.1 ± 0.4	⋯	M6.3 ± 1.1	M7.7 ± 0.5	M8
G 196−3B	L3.0	C09	R98, K01	A07	L4.0:	L4.0:	L3.5 ± 0.4	L3.1 ± 0.8	L4.4 ± 1.1	⋯	L3
2MASS J10220489+0200477	M9.0β	R08, F12	R08, K08	A13	M9.5	L0.0	M8.9 ± 0.4	⋯	M9.5 ± 1.1	M9.1 ± 0.5	M9
2MASS J10224821+5825453	L1.0γ	R08	R08, C09	A13	L1.5	L1.0	L0.8 ± 0.4	L0.8 ± 0.8	L1.8 ± 1.1	L1.2 ± 0.5	L1
2MASS J10452400−0149576	L1.0	C03	S10	A13	L0.0	L1.0	L1.1 ± 0.4	L1.2 ± 0.8	L0.5 ± 1.1	L0.9 ± 0.5	L1
TWA 28 (SSSPM J1102−3431)	M8.5	S05	S05	A13	M9.5	M9.0	M8.2 ± 0.4	⋯	L0.2 ± 1.1	M8.8 ± 0.5	M9
TWA 5B (CD−33 7795B)	⋯	⋯	W99	P12	M9.0:	M8.0	M9.0 ± 0.4	⋯	L1.7 ± 1.1	M9.0 ± 0.5	M9
TWA 8B (2M J1132−26)	M5.0	T03	W99	A09	M6.0	M6.0	M6.0 ± 0.4	⋯	M6.9 ± 1.1	M5.3 ± 0.5	M6
TWA 26 (2M J1139−31)	M9.0	R08	G02	Lu07	M8.5	M9.0	M8.9 ± 0.4	⋯	L0.7 ± 1.1	M8.7 ± 0.5	M9
TWA 27A (2M J1207−39A)	M8.0	G02	G02	A13	M9.0	M8.0	M8.1 ± 0.4	⋯	M9.4 ± 1.1	M7.7 ± 0.5	M8
TWA 11C (2M J1235−39)	M4.5	Ka08	Ka08, W1	A13	M4.5	M5.0	M5.1 ± 0.4	⋯	M5.5 ± 1.1	M4.5 ± 0.5	M5
2MASS J14112131−2119503	M9.0	C03	R09	A13	M8.0	M8.5	M8.3 ± 0.4	⋯	M8.7 ± 1.1	M8.0 ± 0.5	M8
2MASS J15474719−2423493	M9.0	R08	R08, K08	A13	M9.5	L0.0	M9.3 ± 0.4	M7.9 ± 0.8	M9.7 ± 1.1	M9.4 ± 0.5	L0
2MASS J17260007+1538190	L3.0β	C09	C09	M03	L3.0	⋯	⋯	⋯	L2.1 ± 1.1	⋯	L3
2MASS J17312974+2721233	L0.0	R08	S10	A13	L0.0	L0.0	M9.2 ± 0.4	M9.0 ± 0.8	M9.8 ± 1.1	M9.3 ± 0.5	L0
2MASS J19355595−2846343	M9.0	R08	M10	A13	L0.0	L0.0	M9.2 ± 0.5	⋯	M9.6 ± 1.1	M8.6 ± 0.6	M9
2MASS J20575409−0252302	L1.5	C03	C03, S10	A13	L1.0	L3.0	L2.0 ± 0.4	L1.5 ± 0.8	L2.0 ± 1.1	L1.1 ± 0.5	L2
2MASS J22443167+2043433	L6.5	K08	K08	M03	L7.0	L5.5:	⋯	L6.1 ± 0.8	⋯	⋯	L6
2MASS J23224684−3133231	L0.0β	R08	F12	A13	L1.0	L2.0	L1.6 ± 0.4	L1.8 ± 0.8	L4.0 ± 1.1	L1.8 ± 0.5	L2

Notes.
[a] Uncertainties in the spectral types are ±1 subtype except where noted by a colon, which indicates an uncertainty of ±2 subtypes.
[b] More commonly known as PC 0025+04.

References. A07: Allers et al. 2007; A09: Allers et al. 2009; A10: Allers et al. 2010; A13: This Work; B06: Burgasser & McElwain 2006; B08: Burgasser et al. 2008; B10: Burgasser et al. 2010; C03: Cruz et al. 2003; C04: Cruz et al. 2004; C06: Chiu et al. 2006; C07: Cruz et al. 2007; C09: Cruz et al. 2009; Ch04: Chauvin et al. 2004; Ch05a: Chauvin et al. 2005a; Ch05b: Chauvin et al. 2005b; F09: Faherty et al. 2009; F12: Faherty et al. 2012; F13: Faherty et al. 2013; G02: Gizis 2002; G11: Geißler et al. 2011; G12: Gizis et al. 2012; H02: Hawley et al. 2002; K95: Kirkpatrick et al. 1995; K00: Kirkpatrick et al. 2000; K01: Kirkpatrick et al. 2001; K06: Kirkpatrick et al. 2006; K08: Kirkpatrick et al. 2008; K10: Kirkpatrick et al. 2010; Ka08: Kastner et al. 2008; L07: Looper et al. 2007; L08: Looper et al. 2008; Lu07: (K. L. Luhman 2007, private communication); M99a: Martín et al. 1999a; M99b: Martín et al. 1999b; M03: McLean et al. 2003; M08: Metchev et al. 2008; M10: Martín et al. 2010; P12: Patience et al. 2012; R98: Rebolo et al. 1998; R02: Reid et al. 2002; R08: Reid et al. 2008; R09: Reiners & Basri 2009; R10: Rice et al. 2010b; S03: Salim et al. 2003; S05: Scholz et al. 2005; S07: Schmidt et al. 2007; S09: Shkolnik et al. 2009; S10: Seifahrt et al. 2010; T03: Torres et al. 2003; T97: Thackrah et al. 1997; T98: Tinney & Reid 1998; W99: Webb et al. 1999; W08: West et al. 2008; W11: Wahhaj et al. 2011; W13: Weinberger et al. 2013.

optical spectroscopy. Cruz et al. (2009) propose optical gravity classifications of δ, γ, and β and suggest that they correspond to ages of ∼1, ∼10, and ∼100 Myr, respectively. Included in our sample are nine spectra for members of the ∼12 Myr old TW Hydra moving group (hereinafter TWA). Six spectra in our sample are substellar companions to young stars.

In addition to our sample of young objects, we also use a sample of field dwarfs having no known spectral peculiarities to establish a normal gravity sequence. At low spectral resolution ($R \approx 100$), we include the spectra of field dwarf standards from Geißler et al. (2011) and Kirkpatrick et al. (2010) as well as the spectral templates from Burgasser et al. (2010). At moderate resolution ($R \approx 750$–2000), we use spectra from the IRTF Spectral Library (Cushing et al. 2005).

We also include published spectra of objects thought to have dusty photospheres (Kirkpatrick et al. 2010; Looper et al. 2008). These objects have peculiar near-IR spectra and very red near-IR colors but are thought to have normal gravity based on their optical spectra. These dusty objects provide an important test for our indices and classification system. Our gravity-sensitive indicators should show these dusty objects to have normal gravities, similar to field dwarfs.

3. IRTF/SpeX NEAR-IR SPECTROSCOPY

We obtained spectroscopy of our targets using the SpeX spectrograph (Rayner et al. 2003) on the 3 m NASA Infrared Telescope Facility (hereinafter IRTF) located on the summit of Mauna Kea, Hawaii. Our sample includes observations taken using the 0.8–2.4 μm moderate-resolution ($R \approx 750$–2000), cross-dispersed mode (hereinafter SXD) and the 0.8–2.5 μm low-resolution ($R \approx 100$), prism mode (hereinafter PRZ). The instrument configurations, integration times and observation dates for each of our targets are listed in Table 2. Data reduction was performed using the facility reduction pipeline, Spextool (Cushing et al. 2004). We observed A0 stars proximate in time and sky position to our science targets and used these data to correct for telluric absorption following the method described in Vacca et al. (2003). We also added published near-IR spectra to

Table 2
Log of SpeX Observations

Object	Date (UT)	Mode	Slit Width (arcsec)	Exposure Time (s)	A0 V Standard
2MASS J00034227−2822410	2006 Sep 13	SXD	0.5	720	HD 141
2MASS J00192626+4614078	2010 Sep 10	SXD	0.5	480	HD 1561
2MASS J00274197+0503417	2012 Sep 20	PRZ	0.5	2160	HD 1663
2MASS J00325584−4405058	2008 Aug 15	PRZ	0.5	1800	HD 8977
2MASS J00332386−1521309	2008 Nov 29	PRZ	0.5	900	HD 222332
2MASS J00452143+1634446	2008 Aug 15	SXD	0.8	1440	HD 7215
SERC 296A	2006 Nov 19	SXD	0.5	1200	HD18546
2MASS J02292794−0053282	2012 Sep 20	PRZ	0.5	1080	HD 18571
2MASS J02411151−0326587	2008 Dec 1	PRZ	0.5	2160	HD 13936
2MASSI J0253597+320637	2011 Sep 21	SXD	0.8	1200	HD 19600
2MASS J03140344+1603056	2012 Jul 6	SXD	0.8	360	HD21038
2MASS J03350208+2342356	2006 Dec 19	SXD	0.8	1920	HD 23258
2MASS J03350208+2342356	2008 Nov 30	PRZ	0.5	900	HD 23258
LP 944−20	2006 Nov 19	SXD	0.3	720	HD18735
2MASS J03552337+1133437	2008 Aug 15	SXD	0.8	1800	HD 25175
2MASS J04070752+1546457	2008 Aug 15	PRZ	0.5	1440	HD 25175
2MASS J04221413+1530525	2006 Dec 19	SXD	0.8	1200	HD 25175
2MASS J04351455−1414468	2008 Sep 24	SXD	0.8	600	HD 25754
2MASS J04362788−4114465	2012 Sep 20	SXD	0.5	2160	HD 27873
2MASS J04433761+0002051	2011 Sep 21	SXD	0.8	1200	HD34317
2MASS J05184616−2756457	2008 Sep 24	PRZ	0.5	1800	HD 34997
2MASS J05361998−1920396	2012 Sep 20	PRZ	0.5	960	HD 35647
2MASS J05575096−1359503	2008 Jan 27	PRZ	0.3	600	HD 41649
2MASS J05575096−1359503	2008 Nov 30	SXD	0.5	5400	HD 41085
2MASS J06023045+3910592	2010 Mar 3	SXD	0.8	720	HD 45105
2MASS J06085283−2753583	2006 Dec 19	PRZ	0.8	1200	HD 43070
2MASS J06195260−2903592	2008 Nov 28	PRZ	0.5	1200	HD 46680
LP 423−31	2006 Nov 19	SXD	0.3	360	85 Gem
2MASS J08040580+6153336	2008 Nov 27	SXD	0.5	1200	30 Cam
2MASS J10220489+0200477	2008 Nov 28	SXD	0.5	2400	HD 79752
2MASS J10224821+5825453	2008 Nov 27	SXD	0.5	2160	39 UMa
2MASS J10452400−0149576	2012 Apr 30	SXD	0.8	720	HD101122
DENIS-P J104731.1−181558	2012 Apr 30	PRZ	0.8	3600	HD 92079
TWA 28	2007 Mar 25	SXD	0.5	1200	HD 99062
TWA 27A	2007 Mar 26	SXD	0.5	900	HD 99062
TWA 11C	2009 Jul 18	SXD	0.5	600	HD 108481
2MASS J14112131−2119503	2010 Mar 3	SXD	0.5	720	HD 125299
2MASS J15474719−2423493	2009 May 6	PRZ	0.5	600	HD 142705
2MASS J15474719−2423493	2009 Jul 2	SXD	0.5	2160	HD 141091
2MASS J15515237+0941148	2009 May 5	PRZ	0.5	1440	26 Ser
2MASS J15525906+2948485	2009 Jul 18	PRZ	0.5	1440	26 Ser
2MASS J16154255+4953211	2008 Aug 15	PRZ	0.5	1800	55 Dra
2MASS J17073334+4301304	2009 May 7	PRZ	0.5	1080	CCDM 18015+4019AB
2MASS J17111353+2326333	2012 Sep 26	PRZ	0.5	240	GAT 7
2MASS J17260007+1538190	2009 May 6	PRZ	0.5	1200	HD 165029
2MASS J17312974+2721233	2010 Mar 3	PRZ	0.5	240	HD 165029
2MASS J17312974+2721233	2010 Apr 23	SXD	0.8	1260	HD 165029
2MASS J19355595−2846343	2009 Jul 2	PRZ	0.5	720	HD 190285
2MASS J19355595−2846343	2011 Jul 8	SXD	0.8	2640	HD 184533
2MASS J20135152−2806020	2009 Jul 2	PRZ	0.5	600	HD 190285
2MASS J20575409−0252302	2006 Nov 18	SXD	0.5	720	HD 19870
2MASS J22081363+2921215	2008 Nov 29	PRZ	0.5	1680	HD 210501
2MASS J22134491−2136079	2011 Sep 8	PRZ	0.8	720	HD 194272
2MASS J23224684−3133231	2008 Nov 28	SXD	0.8	1200	HD 225200

our sample (references listed in Table 1). Spectra of our sample are displayed in Figures 1 and 2.

4. ANALYSIS

4.1. Spectral Typing

Spectral classification is primarily based on visual examination of a large sample of objects in a common wavelength range and then choosing specific objects to serve as the defining templates for the spectral classes and subclasses. This is the heart of the long-established Morgan–Keenan system, spanning on the two parameters of overall spectral appearance (i.e., spectral type) and luminosity class (Morgan et al. 1943). A visual-based approach has several advantages, most notably that the ensemble morphological information of the data is best captured by human judgement. Practically speaking, a well-constructed
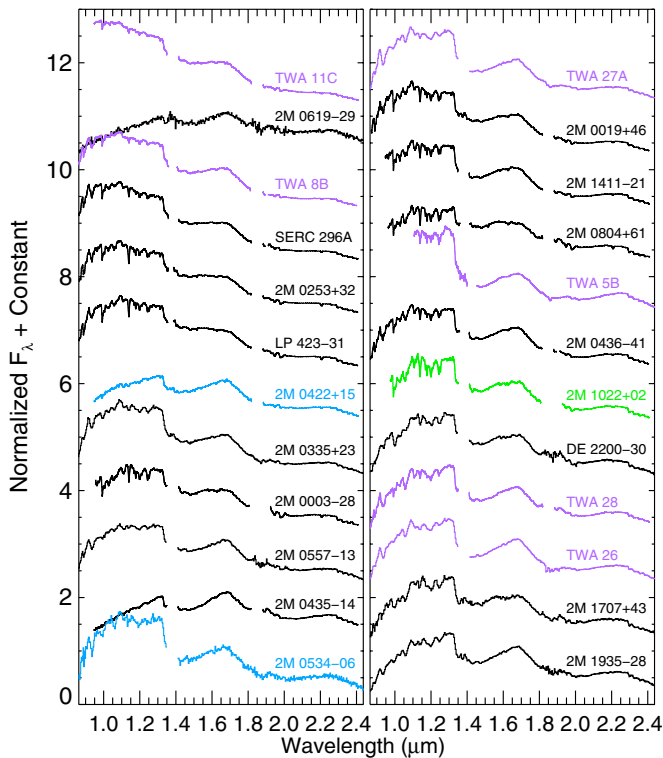
Figure 1. Near-IR spectra of the M dwarfs in our sample. Moderate-resolution spectra have been smoothed with a Gaussian to a resolution of ∼200 for display purposes. For objects having both low- and moderate-resolution spectra, the low-resolution spectrum is displayed. Spectra plotted in purple are known members of the ∼12 Myr old TW Hydra Association (TWA). Spectra plotted in blue have optical gravity classifications of γ or δ. Spectra plotted in green have optical gravity classifications of β. Objects plotted in black have no available optical gravity classification.

(A color version of this figure is available in the online journal.)

sequence should result in a smooth progression of changes in spectral morphology (e.g., see discussion in Kirkpatrick 2005).

For field late-M and L dwarfs, there exist well-established spectral classification systems for optical (far-red) spectra (Boeshaar & Tyson 1985; Kirkpatrick et al. 1999). At these wavelengths and spectral types, multiple absorption features are gravity-sensitive and have been used to identify young objects in young clusters and the field (e.g., Martín et al. 1999a; Slesnick et al. 2004; Kirkpatrick et al. 2006). Cruz et al. (2009) have proposed a formal system for classifying young L0–L5 dwarfs at optical wavelengths based on template objects spanning three gravity classes (α, β, and γ). Optical spectral types for our sample are listed in Table 1 and typically have an uncertainty of 1 subtype.

However, young ultracool dwarfs lack any classification system at the near-IR wavelengths, both for spectral type and gravity. Development of such a system is compelling for two reasons. Late-M and L dwarfs are brightest in the near-IR, making spectroscopic follow-up possible with moderate-aperture (3–4 m) telescopes. Moreover, previous studies have shown that the appearance of the near-IR continuum is strongly gravity-dependent, even at low ($R \sim 100$) spectral resolution (e.g., Lucas et al. 2001; Allers et al. 2007; Lodieu et al. 2008).

The major obstacle to a near-IR system is the heterogeneous nature of ultracool dwarf spectra at these wavelengths. Unlike the smooth sequence of optical spectra, the progression of near-IR spectra for L dwarfs is far more irregular, especially at H and K band (e.g., Kirkpatrick 2005). At fixed optical spectral type,

there is also a large spread in the near-IR colors, believed to be due to the influence of gravity, metallicity, and photospheric condensate variations (e.g., Knapp et al. 2004; Stephens et al. 2009). Therefore the overall shapes of the near-IR SEDs do not follow a smooth sequence, inhibiting the traditional approach of defining actual template objects.

Our large collection of spectra provides a unique opportunity to examine classification of ultracool dwarfs in the near-IR. We follow a two-pronged approach.

1. First, we apply visual classification methods by comparing our sample with the set of J-band spectral standards proposed by Kirkpatrick et al. (2010). They have found classification is possible for field objects in this restricted wavelength regime, with the resulting near-IR types being very similar to optical types for the same objects. *We show here that qualitative (visual-based) classification also works for young L dwarfs, though there is a ≈1 subclass systematic shift between the near-IR and optical types.*

2. Then, we consider a quantitative (index-based) approach to classifying spectral types and gravities. Previous near-IR studies have shown that the H_2O absorption bands, as measured by flux ratios (indices), are well correlated with optical spectral type (e.g., Reid et al. 2001; Geballe et al. 2002; McLean et al. 2003). While this approach is philosophically different from visual classification, these studies demonstrate that prominent near-IR features do change in the same fashion as the overall optical spectrum, i.e., they track similar physical changes. (In addition, even visually based systems often rely on indices as a practical recipe for classification, e.g., the approach of Kirkpatrick et al. (2000) for L dwarfs.) So while the overall issues with near-IR classification are not solved, it is possible to access information about the underlying physical properties of L dwarfs. Similar to previous studies for old field objects, *we show that well-chosen indices in the near-IR successfully correlate with the spectral type and gravity designations in the optical, allowing us to classify near-IR spectra in a practical and useful fashion.*

4.1.1. Visual Classification

We first compared our spectra of young objects with field dwarf near-IR spectral standards from Kirkpatrick et al. (2010). Not surprisingly, the entire 0.8–2.5 μm spectra of young objects are not well matched by older field dwarfs, in part due to the redder near-IR colors of young objects (Kirkpatrick et al. 2008). In some spectral regions, however, the continuum shape is sensitive to spectral type with little dependence on gravity. In particular, we used the 1.07–1.40 μm and 1.90–2.20 μm wavelength regions to determine J-band and K-band spectral types by visual comparison to field dwarf standards (Figure 3). For each spectrum in our sample, we over-plotted the spectra of field dwarf standards (normalized over the comparison wavelength region) and qualitatively determined which standard best matched the continuum shape of our object. If two standard spectra provided similar matches, we assigned the spectral type intermediate to the two standards, e.g., if the L0 and L1 standards provided equally good fits, we assigned a spectral type of L0.5. For the majority of our objects, selecting a standard with 1 subtype difference compared to the best-fitting standard provided a noticeably poorer fit. Thus, we assign an uncertainty of 1 subtype to our visual classifications. For objects which had either particularly noisy or peculiar spectra, several field dwarf
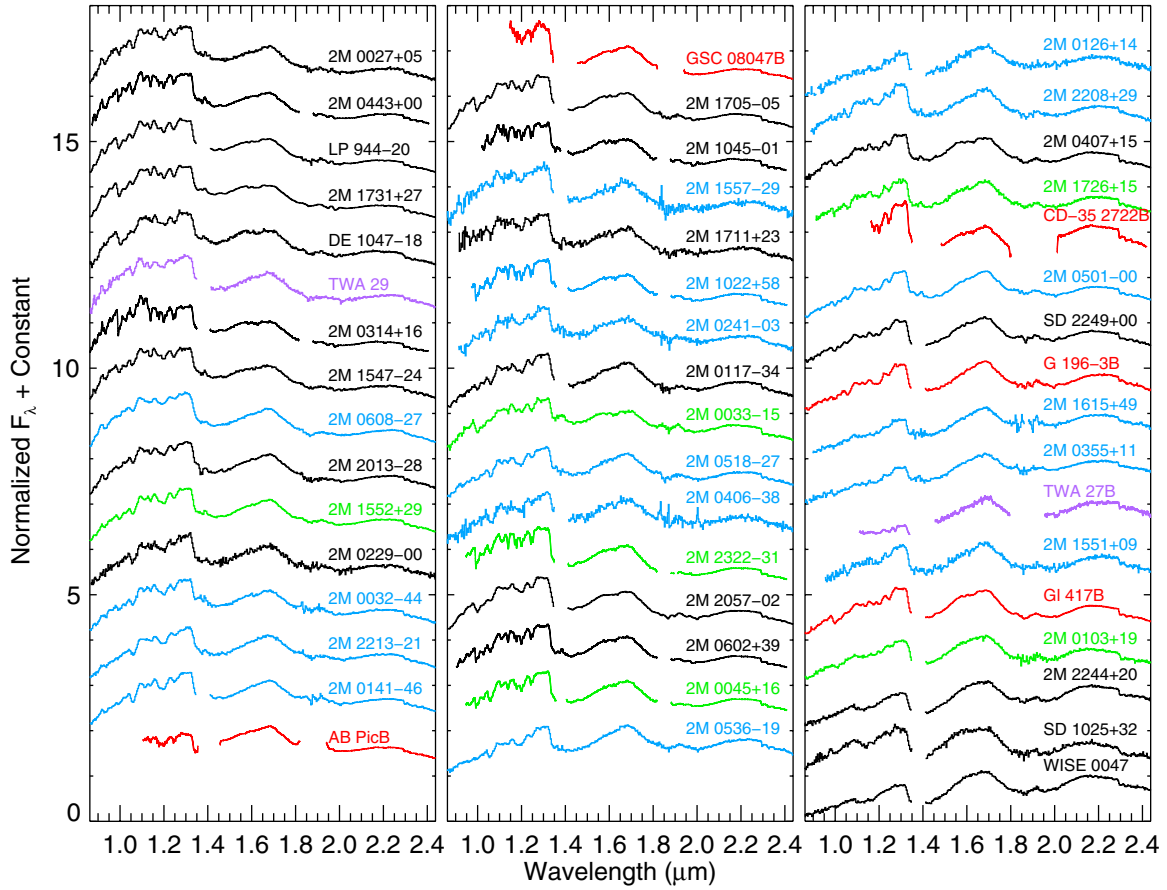
Figure 2. Near-IR spectra of the L dwarfs in our sample. Color coding is the same as for Figure 1, and young companion spectra are displayed in red.
(A color version of this figure is available in the online journal.)
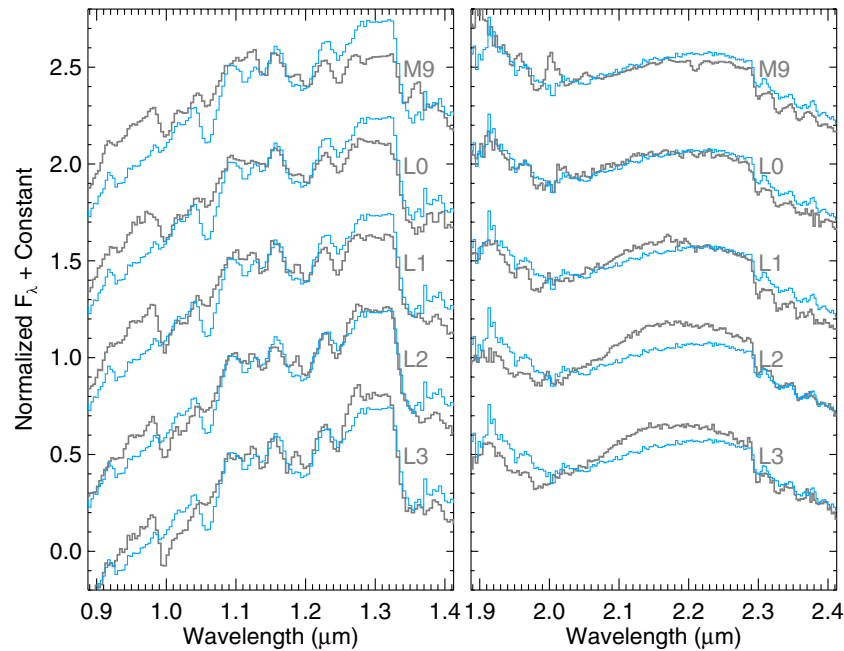
Figure 3. An example of visual classification using the spectrum of 2M 0141−46, which is optically classified as L0γ (Cruz et al. 2009). The spectrum of 2M 0141−46 (Kirkpatrick et al. 2006) is plotted in blue. Spectra of field dwarf standards (Kirkpatrick et al. 2010) are plotted in gray. Based on visual comparison of the 1.07–1.40 μm spectrum of 2M 0141−46 to field dwarf standards, we assign a J-band spectral type of L2. The K-band spectral type of 2M 0141−46, L0, is assigned based on the best-matching field standard at wavelengths of 1.90–2.20 μm.

(A color version of this figure is available in the online journal.)
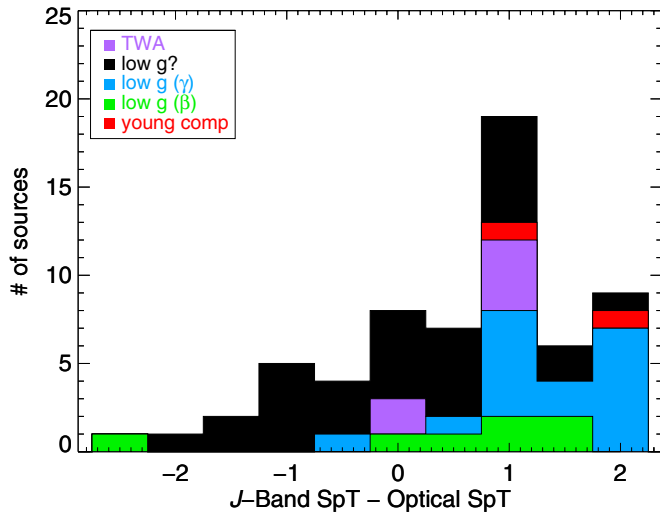
Figure 4. Histogram showing the difference between our *J*-band visual spectral types and published spectral types. The *J*-band visual spectral types for young objects tend to be later than their optical spectral types, particularly among the lowest gravity objects in our sample (optical classifications of γ and TWA members).

(A color version of this figure is available in the online journal.)

Figure 5. Histogram showing the difference between our *K*-band visual spectral types and published optical spectral types. For the majority of our sample, our *K*-band spectral types agree with optical spectral types to within our uncertainty (± 1 subtype).

(A color version of this figure is available in the online journal.)

standards provided equally good fits, thus uncertainties of ± 2 subtypes were assigned to their visual classification.

To test for any gravity dependence of our visual spectral typing, we compared the near-IR spectral types of ~ 10 Myr old objects in our sample (TWA members and objects with optical gravity classifications of γ) to their optical spectral types. On average, the *J*-band spectral types of ~ 10 Myr old objects are 1.3 subtypes later than their corresponding optical spectral types. The *K*-band spectral types for low-gravity objects are, on average, 0.1 subtypes earlier than their corresponding optical spectral types. *Determining near-IR spectral types for young objects based on visual comparison to field dwarfs will lead to near-IR types that are slightly later than their optical spectral types.* In addition to visually comparing our spectra to the IR standards, we also computed reduced χ^2 for the 1.07–1.40 μm and 1.90–2.20 μm wavelength regions to assign spectral types based on the best matching standard. The spectral types determined from the minimum χ^2 value agreed to within the uncertainties with the spectral types determined by visual classification (± 1 subtype). Minimum reduced χ^2 values for fitting spectra of field standards to ~ 10 Myr old objects were typically ~ 30 for *J*-band fits and ~ 7 for *K*-band fits. The large values for reduced χ^2 are a result of the poor match between field dwarf standards and young field objects. Figures 4 and 5 show the differences between our *J*- and *K*-band visual spectral types and published optical spectral types.

4.1.2. Index-based Classification

Another method of determining spectral type is using spectral indices. This method has the potential advantage of measuring spectral features which are well correlated with the overall spectral morphology (type) of the object, while avoiding wavelength regions containing broad, gravity-sensitive features. We calculated many published spectral type-sensitive indices (Tokunaga & Kobayashi 1999; Cushing et al. 2000; Testi et al. 2001; Geballe et al. 2002; McLean et al. 2003; Slesnick et al. 2004; Allers et al. 2007; Weights et al. 2009; Covey et al. 2010; Scholz et al. 2012) for the objects in our sample. Most of these
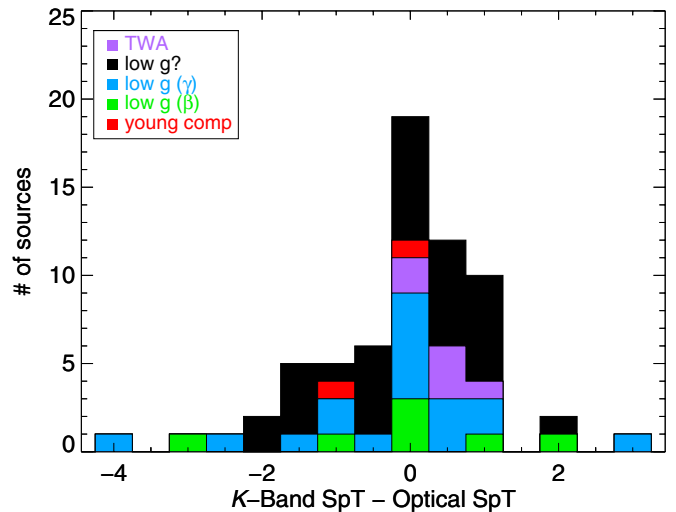
spectral-type sensitive indices were developed to correlate with optical spectral types. The majority of spectral type-sensitive indices were either found to be gravity-sensitive (i.e., young dwarfs and field dwarfs having very discrepant index–SpT relations) or were only sensitive over a narrow range in spectral type. Overall, we find that the H_2O (Allers et al. 2007), H_2O-1, H_2O-2 (Slesnick et al. 2004), and H_2OD[4] (McLean et al. 2003) indices are spectral type sensitive and gravity-insensitive over a broad range in spectral type. For these four indices, we fit index versus optical spectral type for field dwarfs with a third-degree polynomial and use the scatter about the fit as the uncertainty in the index–SpT relation (Figure 6). The polynomial fits and scatter in the index–SpT relations, along with the range of spectral type sensitivity, are presented for each index in Table 3. Table 1 presents the spectral types calculated from these indices for our sample of young objects. Uncertainties in the index-derived spectral types were determined using a Monte Carlo approach to account for uncertainties in the index calculations from each spectrum. These were then added in quadrature to the rms SpT scatter in the index–SpT relations (Table 3).

4.1.3. Final Near-IR Spectral Types

To arrive at final near-IR spectral types, we take the weighted mean of all of the spectral types determined using indices and visual comparison. For many of our objects, this results in the visual spectral types having little effect on the final spectral type determination. We round the final spectral type to the nearest integer subtype. Uncertainties in the weighted mean spectral type were 0.3–0.9 subtypes, thus we adopt a conservative uncertainty of 1 subtype for our near-IR spectral types. The near-IR spectral types of our sample are, on average, 0.07 subtypes earlier than their published optical spectral types. For the ~ 10 Myr old objects in our sample, their near-IR spectral types are, on average, identical to their published optical spectral types. Figure 7 shows the differences between our near-IR spectral types and published optical spectral types. The vast

---

[4] The H_2OD index (McLean et al. 2003) uses wavelength windows that are smaller than a resolution element of our low-resolution spectra, so we widened the index windows to 0.013 μm (Table 3).
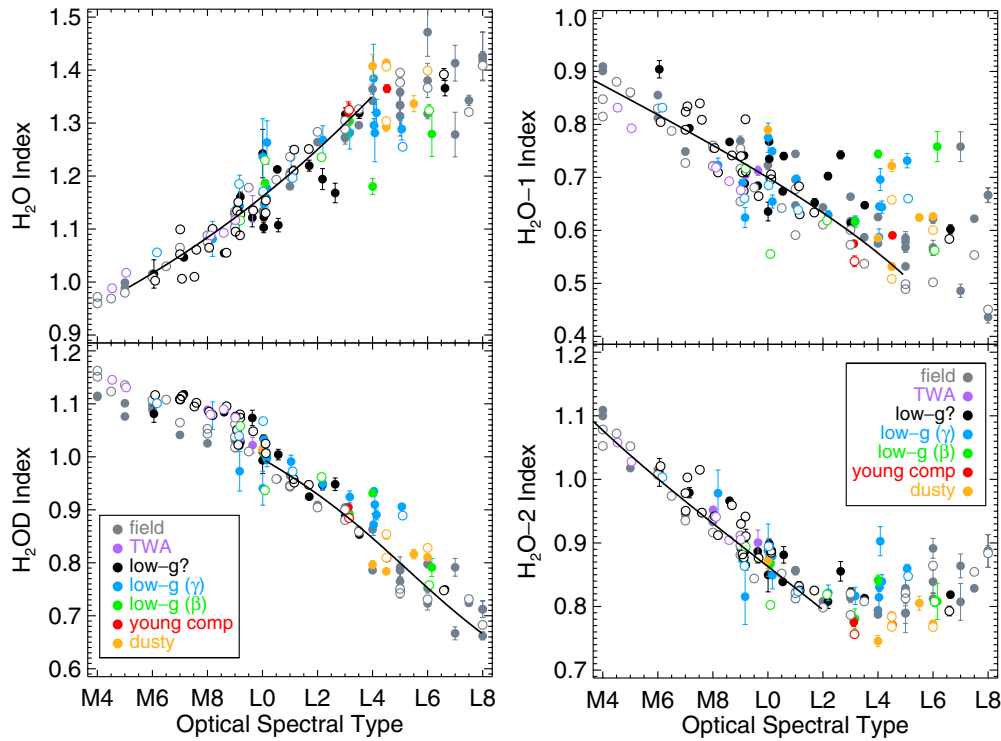
Figure 6. Spectral type sensitive indices as a function of optical spectral type for four near-IR indices showing negligible gravity dependence. Data and references are presented in Table 1. Normal field dwarfs are plotted as gray points. Purple points represent members of the TW Hydra moving group (~10 Myr old). Objects in our sample with an optical gravity classification of β are displayed as green points and those having an optical classification of γ are displayed as blue points. Black points (low g?) show objects in our sample having no optical gravity classification. Red points represent young companions to stars. Objects with normal gravity but thought to have dusty photospheres are displayed in orange. Filled circles show index values calculated from low-resolution ($R \approx 100$) spectra, and open circles show values calculated from moderate-resolution ($R \approx 750$–2000) spectra. The solid black lines are third-degree polynomial fits to index vs. optical spectral type for field dwarfs and are plotted only over the range of spectral type sensitivity for each index. Index definitions, ranges, and polynomial fits are presented in Table 3.

(A color version of this figure is available in the online journal.)

Table 3
Spectral Type Sensitive Indices

Index Definition	Index Ref.	SpT	Coefficients of Polynomial Fits[a]				rms
			c_0	c_1	c_2	c_3	SpT
$H_2O = \frac{\langle F_{\lambda=1.550-1.560}\rangle}{\langle F_{\lambda=1.492-1.502}\rangle}$	Allers et al. (2007)	M5–L4	-83.5437	169.388	-104.424	24.0476	0.390
$H_2OD = \frac{\langle F_{\lambda=1.951-1.977}\rangle}{\langle F_{\lambda=2.062-2.088}\rangle}$	McLean et al. (2003)	L0–L8	79.4477	-202.245	229.884	-97.230	0.757
$H_2O\text{-}1 = \frac{\langle F_{\lambda=1.335-1.345}\rangle}{\langle F_{\lambda=1.295-1.305}\rangle}$	Slesnick et al. (2004)	M4–L5	12.1927	39.3513	-80.7404	28.5982	1.097
$H_2O\text{-}2 = \frac{\langle F_{\lambda=2.035-2.045}\rangle}{\langle F_{\lambda=2.145-2.155}\rangle}$	Slesnick et al. (2004)	M4–L2	10.8822	55.4580	-97.8144	37.5013	0.501

Note. [a] The spectral type is calculated from the polynomial fits as: $SpT = c_0 + c_1(\text{index}) + c_2(\text{index})^2 + c_3(\text{index})^3$.
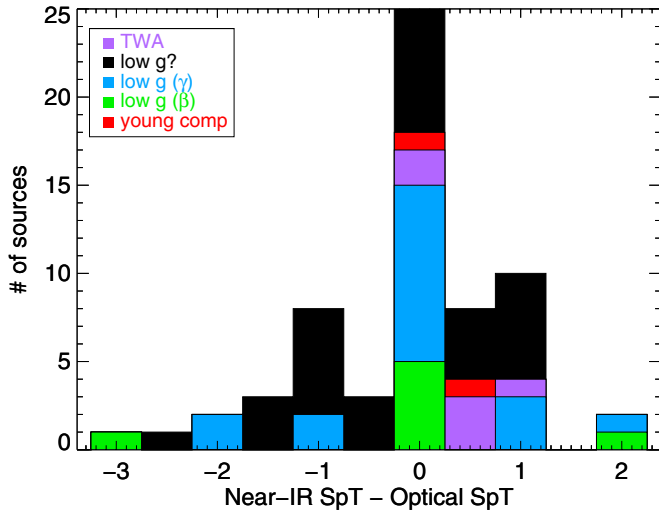
majority (55/64) of near-IR and optical spectral types agree to within 1 subtype. The nine objects having discrepant (by more than 1 subtype) near-IR and optical spectral types do not show a preference for particular optical spectral types, gravities, or near-IR colors. Overall, our method for determining IR spectral types yields results that are consistent with optical spectral types. An additional benefit of our method of spectral typing is that we are not biased by an object's $J - K$ color, which has a large dispersion among the L dwarfs (e.g., Knapp et al. 2004), inhibiting the use of the entire spectrum for visual classification. Figure 8 shows the spectra of objects classified as L3 that have $J - K$ colors ranging from 1.6 to 3.1 mag.

4.2. Surface Gravity Indicators

There are several hallmarks of youth (low gravity) in the 0.9–2.5 μm spectra of late-M and L dwarfs. Gravity-sensitive

features in the near-IR spectra of late-M dwarfs were originally identified by comparison of dwarf and giant spectra (e.g., Kleinmann & Hall 1986; Joyce et al. 1998; Meyer et al. 1998). Not surprisingly, many of these same spectral features are seen in the spectra of young, late-M and early-L type brown dwarfs in star-forming regions (e.g., Lucas et al. 2001; Gorlova et al. 2003; McGovern et al. 2004; Allers et al. 2007; Lodieu et al. 2008). In the current work, we seek to identify and quantify gravity-sensitive features over a broad range in spectral type (M5–L7). Figures 9–11 compare low-resolution spectra of objects having field gravity, intermediate gravity, and very low gravity as determined from optical spectroscopy (see Table 1 for references). At lower gravity, the photosphere lies at lower pressure, which has an effect on several near-IR spectroscopic features. The FeH bands (0.99, 1.20, and 1.55 μm), Na I lines (1.14 and 2.21 μm), and K I (1.17 and 1.25 μm) lines are weaker in young, low-gravity objects than in older field dwarfs.

Figure 7. Histogram showing the difference between our near-IR spectral types and published optical spectral types. For the majority of our sample (55 out of 64 objects having optical spectral types), our near-IR spectral types agree with optical spectral types to within our uncertainty (±1 subtype).

(A color version of this figure is available in the online journal.)

The VO band ($1.06\,\mu$m) is stronger in the spectra of young objects than in older field objects. The continuum shape of the H-band spectra of young objects has a distinctive "triangular" shape, whereas the older field object tends to display more of a "plateau." The K-band continua of young objects (and dusty objects) have a more positive spectral slope from 2.15 to $2.25\,\mu$m than seen in normal field dwarfs of the same spectral type. Figures 12–15 compare the features in moderate-resolution

Table 4
Gravity-sensitive Spectral Indices

Index[a]	λ_{line} (μm)	λ_{cont1} (μm)	λ_{cont2} (μm)	Bandwidth (μm)
FeH$_z$	0.998	0.980	1.022	0.0133
VO$_z$	1.058	1.035	1.087	0.0141
FeH$_J$	1.200	1.192	1.208	0.0024
K I$_J$	1.244	1.220	1.270	0.0166
H-cont	1.560	1.470	1.670	0.0208

Note. [a] The method for calculating indices is described in Section 4.2.1.

J-band spectra for objects of various ages and gravities. At moderate resolution, the equivalent widths (EWs) of Na I and K I are sensitive to gravity. In the following sections, we examine each of these features and determine the utility of these youth indicators as a function of spectral type and resolution.

The youth of ultracool objects has typically been determined by qualitative spectroscopic comparison of the object to field dwarfs. Here, we establish a set of spectral indices that can be used to evaluate the youth of objects in quantitative fashion. Our basic approach to establishing these spectral indices is to center an index on a feature known to be gravity-dependent and adjust the index definition so that ~10 Myr old objects in our sample (TWA members and objects with optical gravity classifications of γ) have index values that are quantitatively distinct from older field dwarfs. Table 4 and Figures 16–19 present our gravity-sensitive indices.

4.2.1. FeH

The near-IR spectra of late-M and L dwarfs contain a wealth of absorption features attributed to FeH bands (McLean et al.
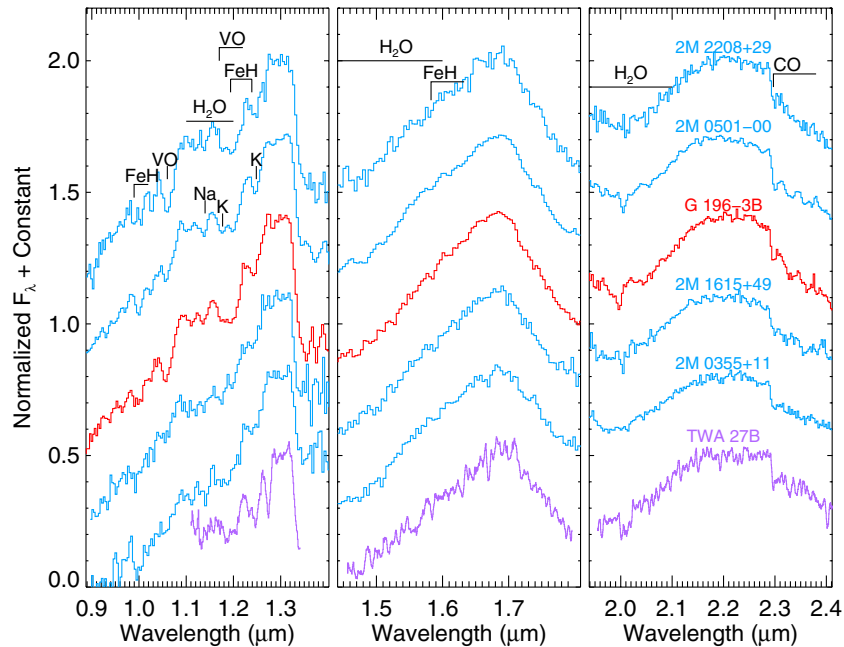

Figure 8. Spectra of objects in our sample having a near-IR spectral type of L3 and classified as VL-G (Section 4.3). Spectra plotted in blue have optical gravity classifications of γ. The red spectrum is G 196−3B, a low-mass companion to a young star. The purple spectrum is TWA 27B (2M 1207b). The J, H, and K bands are plotted separately and normalized by the mean flux at 1.27–1.32, 1.65–1.72, and 2.15–2.25 μm, respectively. The regions of the spectra where indices are used to measure spectral type (1.29–1.35 μm, 1.49–1.56 μm, and 1.95–2.09 μm) are very similar, supporting the L3 IR spectral type assigned to all of them. Despite the similarity of these spectra in the H and K bands, the J-band spectra are more diverse. In particular, 2M 0355+11 and 2M 1615+49 do not have deep 1.06 μm VO features. The spectral shape from ~1.07–1.2 μm also shows noticeable variation. The $J-K$ colors for these objects vary from 1.6 (top spectrum) to 3.1 mag (bottom spectrum).

(A color version of this figure is available in the online journal.)
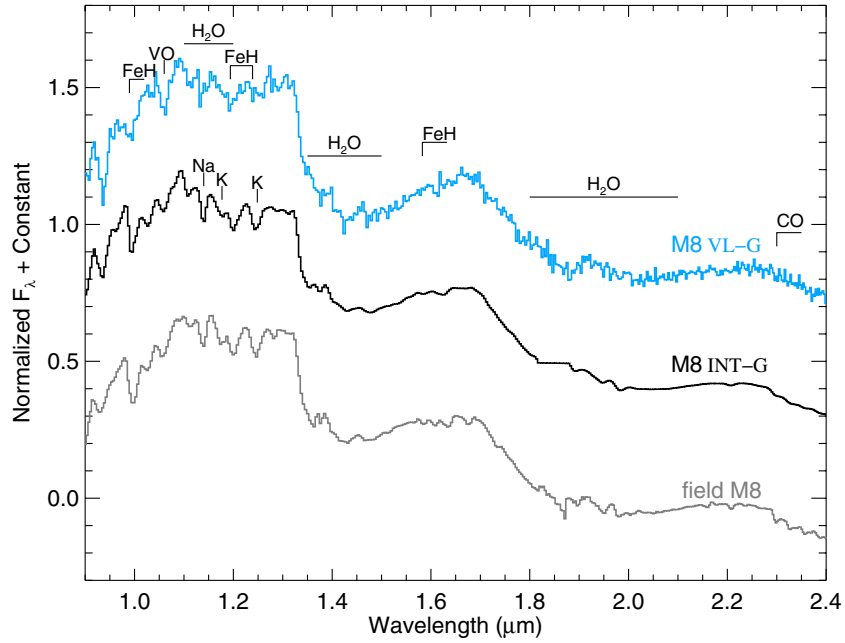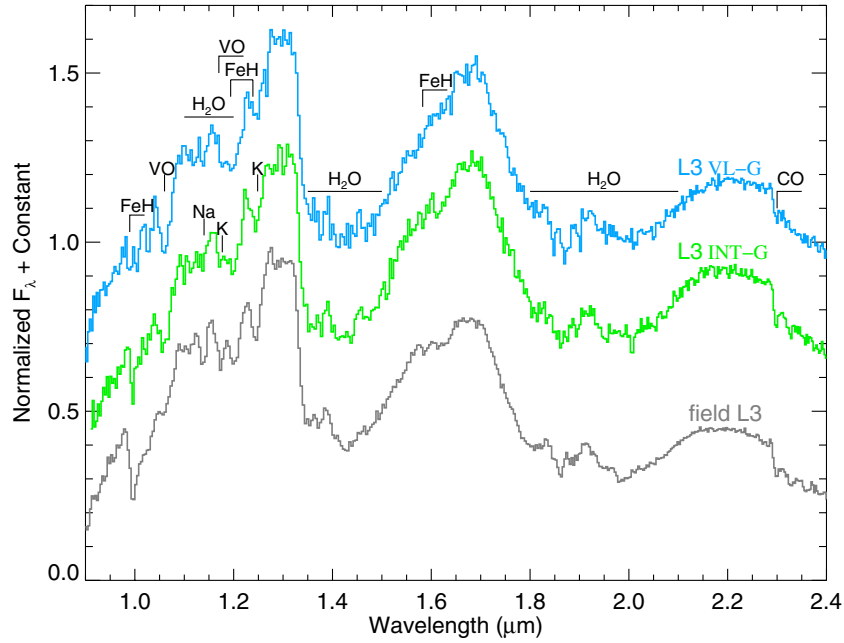
Figure 9. Low-resolution spectra comparing the gravity (age) sensitive features for objects classified as M8 in the near-IR. Details on the near-IR gravity classifications are described in Section 4.3. From its optical spectrum, the VL-G object (blue; 2M 0534−06) is classified as M8γ (Kirkpatrick et al. 2010). The INT-G spectrum is 2M 0019+46 (optical SpT of M8; Cruz et al. 2003), which has been smoothed to a resolution of ~100 to match the low-resolution comparison spectra. The field dwarf spectrum (gray) is vB 10 (Burgasser et al. 2004). The *H*-band continuum shows a distinct triangular shape at low gravities.

(A color version of this figure is available in the online journal.)
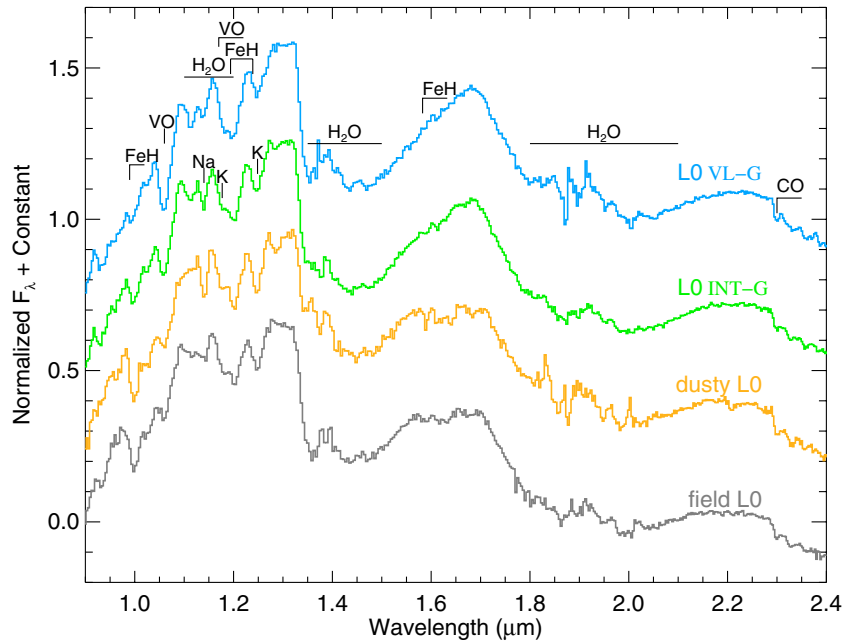
Figure 10. Low-resolution spectra comparing the gravity (age) sensitive features for objects classified as L0 in the near-IR. From their optical spectra, the VL-G object (blue; 2M 0141−46) is classified as L0γ and the INT-G object (green; 2M 1552+29) is classified as L0β (Cruz et al. 2009). The spectrum of the dusty object (orange; 2M 1331+34) is from Kirkpatrick et al. (2010). The field dwarf (gray) is the L0 standard 2M 0345+25 (Burgasser & McElwain 2006). FeH, Na I, and K I features are weaker at lower gravities and VO is stronger. The *H*-band continuum shows a distinct triangular shape at low gravities.

(A color version of this figure is available in the online journal.)

2003; Cushing et al. 2005), which also provide significant atmospheric opacity (Rice et al. 2010a). The most prominent FeH features seen at low resolution are bandheads at 0.99, 1.20, and 1.55 μm. The depth of the FeH absorption features increases steadily through the late-M to early-L spectral types, with spectral types of L2–L3 having the strongest FeH features. For spectral types later than L3, the strengths of the FeH features

decrease. By spectral types of L7, very little FeH is discernable. Low-gravity M and L dwarfs display much weaker FeH bands than field dwarfs of the same spectral type.

We establish the FeH$_z$ index (Table 4 and Figure 16) which measures the depth of the 0.99 μm FeH feature. We optimized the index to be sensitive to gravity for both moderate- and low-resolution spectra by making the wavelength windows for the

Figure 11. Low-resolution spectra comparing the gravity (age) sensitive features for objects classified as L3 in the near-IR. From their optical spectra, the VL-G object (blue; 2M 2208+29) is classified as L3γ and the INT-G object (green; 2M 1726+15) is classified as L3β (Cruz et al. 2009). The field dwarf (gray) is the L3 standard 2M 1506+13 (Burgasser 2007). FeH, Na I, and K I features are weaker at lower gravities and VO is stronger. The *H*-band continuum shows a distinct triangular shape at low gravities.

(A color version of this figure is available in the online journal.)
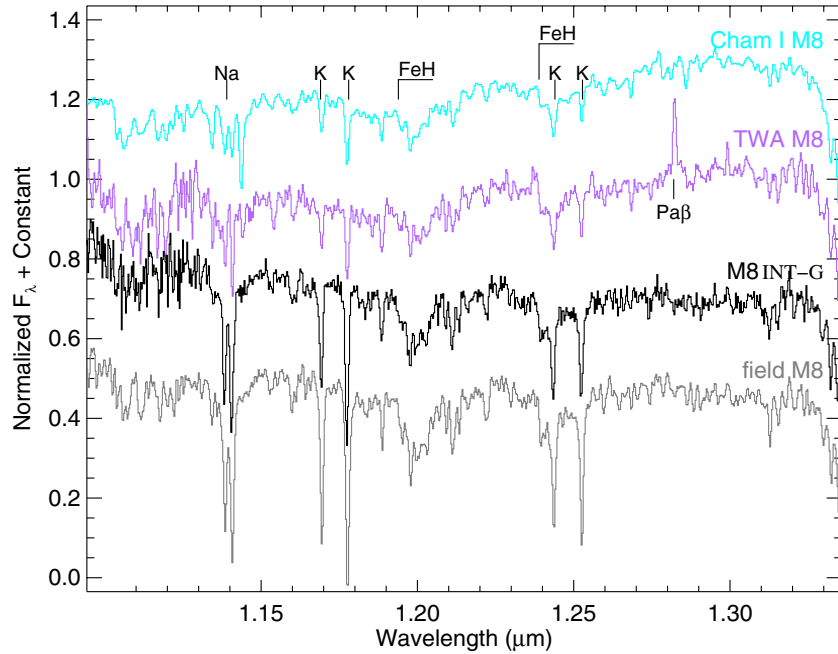
Figure 12. Moderate-resolution spectra comparing the gravity (age) sensitive features in the *J*-band spectra of objects classified as M8 in the near-IR. The TWA M8 spectrum (purple) is TWA 27, which is classified as VL-G. The gravity classification of the INT-G spectrum (2M 0019+46) is described in Section 4.3. Though not an object in our sample, the spectrum of a $\sim$3 Myr old Chamaeleon I M8 (CHSM 17173; K. L. Luhman 2007, private communication) is displayed for comparison. A normal-gravity, field M8 is also displayed (vB 10; Cushing et al. 2005). Young, low-gravity M8s have weaker Na I, K I, and FeH features than normal field M8 dwarfs.

(A color version of this figure is available in the online journal.)

index as wide as a single resolution element for our lowest resolution ($R \sim 75$) spectra. The index is calculated as follows:

$$\text{index} = \left(\frac{\lambda_{\text{line}} - \lambda_{\text{cont1}}}{\lambda_{\text{cont2}} - \lambda_{\text{cont1}}} F_{\text{cont2}} + \frac{\lambda_{\text{cont2}} - \lambda_{\text{line}}}{\lambda_{\text{cont2}} - \lambda_{\text{cont1}}} F_{\text{cont1}} \right) / F_{\text{line}}. \quad (1)$$

The central wavelengths and widths of the line and continuum regions are listed in Table 4. The numerator of the equation

gives the expected flux at the line wavelength (based on a linear interpolation of flux in the continuum windows) if no absorption or emission were present. F_{cont1} is the average of the spectrum (in F_λ units) over a window as wide as the bandwidth listed in Table 4 and centered on λ_{cont1}. F_{cont2} and F_{line} are calculated similarly. Indices calculated using Equation (1) will have values of one for spectra showing no FeH absorption, with higher index values indicating deeper absorption features. Uncertainties in
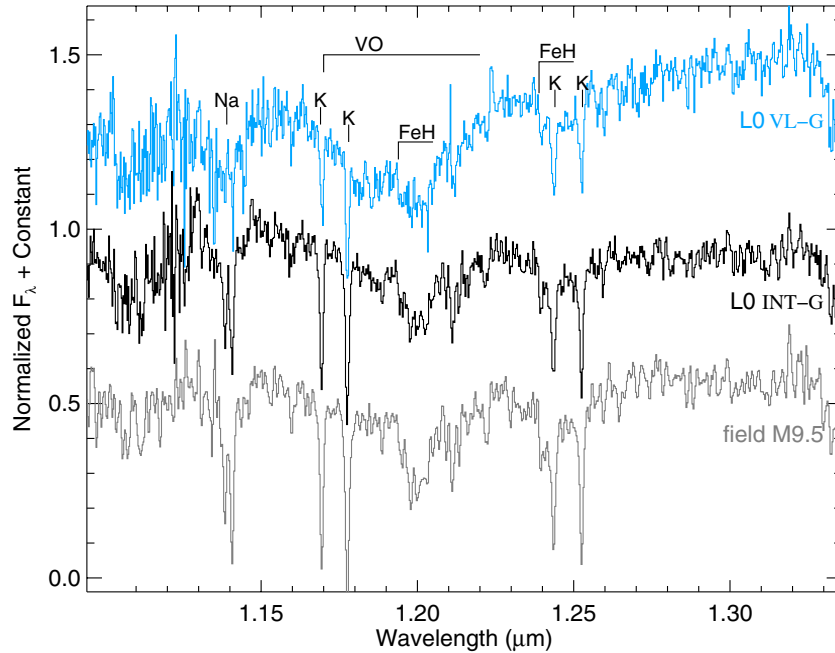
Figure 13. Moderate-resolution spectra comparing the gravity (age) sensitive features in the *J*-band spectra of objects classified as L0 in the near-IR. The L0 VL-G spectrum is 2M 0141−46, which has an optical gravity classification of γ (Kirkpatrick et al. 2006). The gravity classification of the INT-G spectrum (2M 1547−24) is described in Section 4.3. For comparison, the spectrum of a field M9.5 (BRI 0021−0214; Cushing et al. 2005) is displayed. Young, low-gravity L0s have weaker Na I, K I, and FeH features than normal field L0 dwarfs.

(A color version of this figure is available in the online journal.)
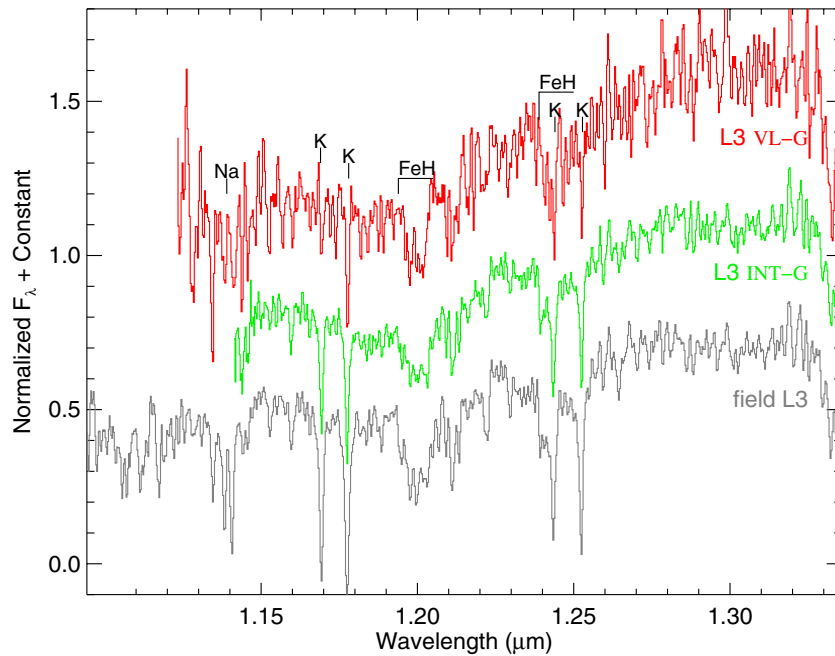
Figure 14. Moderate-resolution spectra comparing the gravity (age) sensitive features in the *J*-band spectra of objects classified as L3 in the near-IR. The L3 VL-G spectrum (red) is G 196−3B, a companion to the 20–300 Myr old M3 star, G 196−3A. The INT-G spectrum (green; 2M 1726+15) has an optical gravity classification of β. For comparison, the spectrum of a field L3 (2M 1506+13; Cushing et al. 2005) is displayed. Young, low-gravity L3s have weaker K I and FeH features than normal field L3 dwarfs.

(A color version of this figure is available in the online journal.)

F_λ per pixel were estimated from the rms scatter about a linear fit to wavelength versus F_λ in the continuum windows. Uncertainties in the index value were calculated assuming that the line region has the same flux uncertainty per pixel as the continuum. We established the expected field dwarf index (black line in Figure 20) and its uncertainty (gray shaded region in

Figure 20) from the mean and standard deviation of the index values of all field dwarfs in ± 1 subtype bins (e.g., the field dwarf index value and uncertainty for L0 are the average and standard deviation of indices for the M9–L1 field dwarfs). Table 5 and Figure 20 present the FeH$_z$ indices calculated for our sample. This index is sensitive to gravity for M6–L7 spectral types.
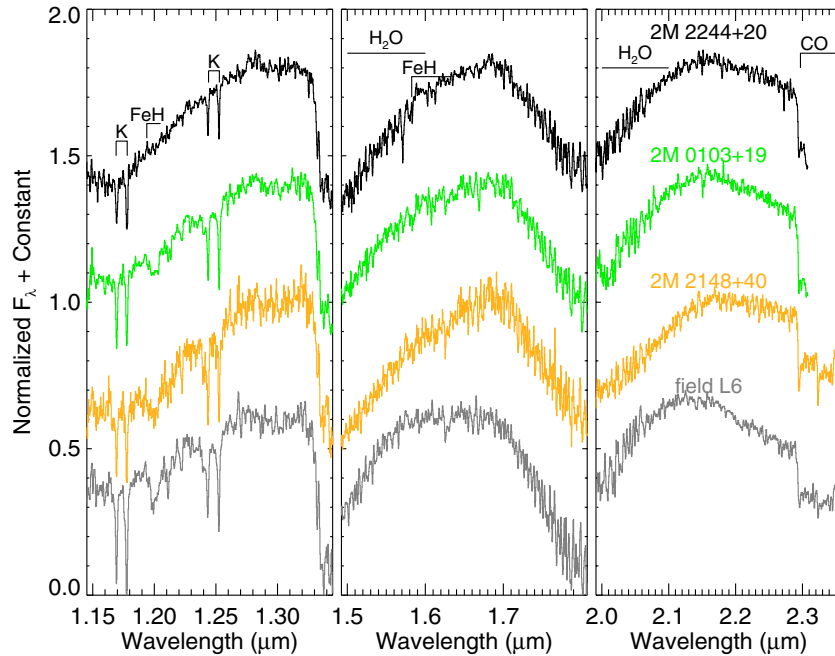
Figure 15. Moderate-resolution spectra comparing low-gravity, dusty, and field L6 dwarfs. The field dwarf L6 spectrum (gray) is 2M 1515+48 from Cushing et al. (2005). The J, H, and K bands are plotted separately and normalized by the mean flux from 1.27–1.32, 1.65–1.72, and 2.15–2.25 μm, respectively. We classify 2M 2244+20 (black) as VL-G and 2M 0103+19 (green) as INT-G. 2M 2148+40 (orange; Looper et al. 2008) is a dusty L6 that does not show signatures of youth in its kinematics or optical spectrum. Based on its IR spectrum, we would classify 2M 2148+40 as FLD-G, as its alkali line EWs and FeH features are consistent with the L6 field dwarf. The H-band continuum shape of 2M 2148+40, however, appears to have the triangular shape indicative of low-gravity. Thus, the H-band continuum shape (and our H-cont index) alone cannot reliably distinguish between low-gravity and dusty photospheres.
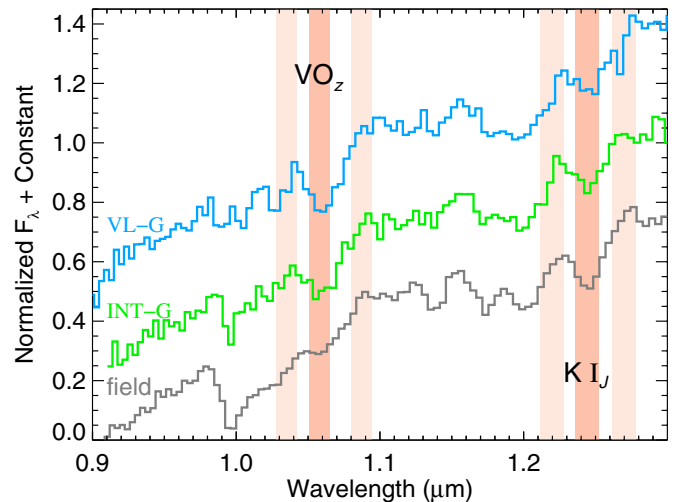
(A color version of this figure is available in the online journal.)
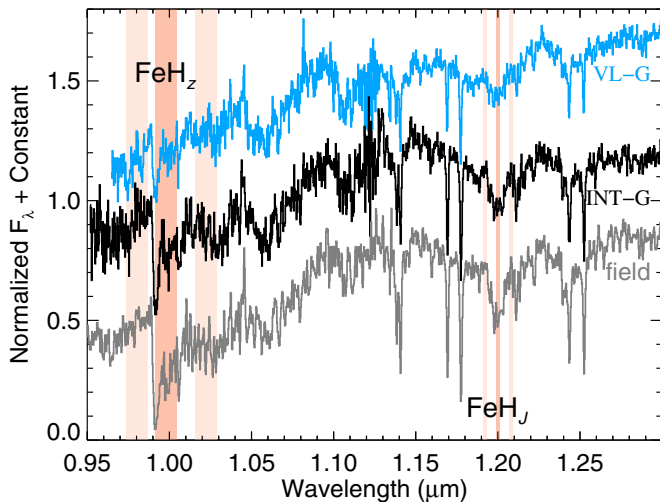
Figure 16. Moderate-resolution spectra showing the line (dark salmon shaded regions) and continuum (light salmon shaded regions) windows for the FeH_z and FeH_J indices (see Table 4 for details). The blue spectrum is 2M 0141−46, an L0 VL-G, which has an optical gravity classification of γ (Kirkpatrick et al. 2006). The black spectrum is the L0 INT-G, 2M 1547−24. For comparison, the spectrum of a field M9.5 (BRI 0021−0214; Cushing et al. 2005) is displayed.

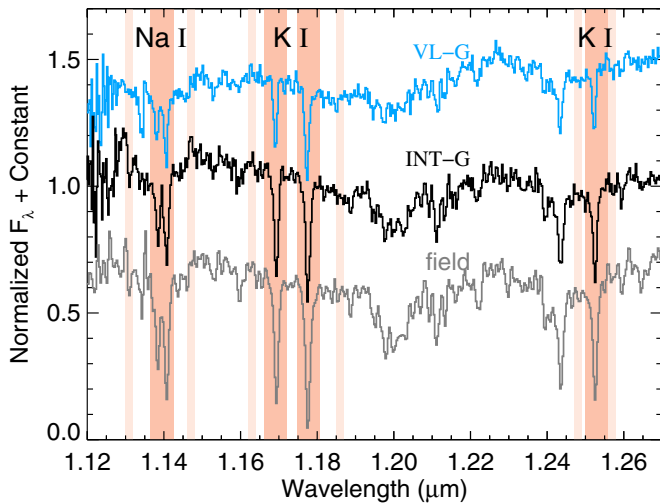(A color version of this figure is available in the online journal.)

Figure 17. Low-resolution spectra showing the line (dark salmon shaded regions) and continuum (light salmon shaded regions) windows for the VO_z and $\mathrm{K\,I}_J$ indices (see Table 4 for details). The blue spectrum is the L3 VL-G object, 2M 2208+29, which is classified as L3γ in the optical. The green spectrum is the L3 INT-G object, 2M 1726+15, which is classified as L3β in the optical (Cruz et al. 2009). The field dwarf (gray; 2M 1506+13) is an L3 standard from Burgasser (2007).

(A color version of this figure is available in the online journal.)

Many of our moderate-resolution spectra do not extend to short enough wavelength to calculate the FeH_z index. To measure the 1.20 μm FeH feature, we created the FeH_J index. At low spectral resolution, the 1.20 μm FeH feature is blended with Fe I, Mg I, and K I, thus the FeH_J index is only appropriate for moderate-resolution spectra. Table 6 and Figure 21 display the FeH_J indices calculated from our moderate-resolution spectra.

The 1.55 μm FeH feature contributes to the measured values of the H-cont index and is discussed in Section 4.2.4.

4.2.2. VO

Condensation effects and higher metal hydride opacities contribute to the weaker strength of vanadium oxide (VO) bands in field dwarfs compared to low-gravity (young) ultracool

Figure 18. Moderate-resolution spectra showing the line (dark salmon shaded regions) and continuum (light salmon shaded regions) windows for alkali line equivalent width calculation (see Table 7 for details). The blue spectrum is 2M 0141−46, an L0 VL-G, which has an optical gravity classification of γ (Kirkpatrick et al. 2006). The black spectrum is the L0 INT-G, 2M 1547−24. For comparison, the spectrum of a field M9.5 (BRI 0021−0214; Cushing et al. 2005) is displayed.

(A color version of this figure is available in the online journal.)
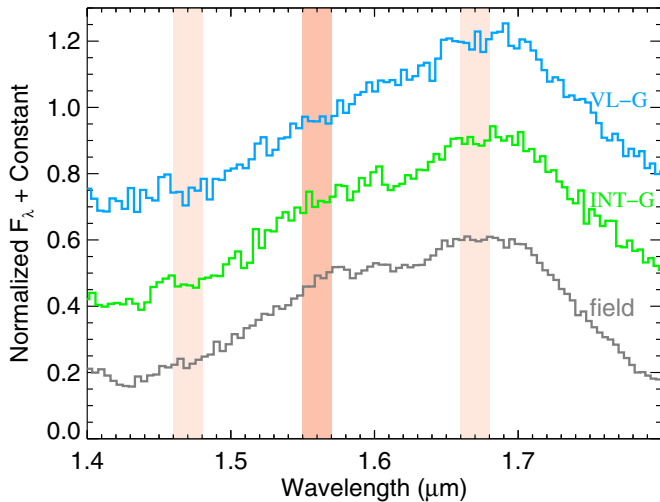
Figure 19. Low-resolution spectra showing the line (dark salmon shaded regions) and continuum (light salmon shaded regions) windows for the H-cont index (see Table 4 for details). The blue spectrum is the L3 VL-G object, 2M 2208+29, which is classified as L3γ in the optical. The green spectrum is the L3 INT-G object, 2M 1726+15, which is classified as L3β in the optical (Cruz et al. 2009). The field dwarf (gray) is the L3 standard 2M 1506+13 (Burgasser 2007).

(A color version of this figure is available in the online journal.)

dwarfs. We established a gravity-sensitive VO_z index (Table 4 and Figure 17), similar to the z–VO index presented in Cushing et al. (2005), but optimized for low-resolution spectra. A larger value of the VO_z index corresponds to deeper 1.06 μm VO absorption. Figure 20 shows the index calculated for our sample, using Equation (1). We established the expected field dwarf index and its uncertainty in the same manner as for the FeH_z index. We find that the 1.06 μm VO feature is an excellent gravity indicator for L0–L4 dwarfs, with the index values for optically classified Lγ dwarfs lying well above the field dwarf sequence. Young, late-M dwarfs also show enhanced VO absorption, but the difference between young M dwarfs and field
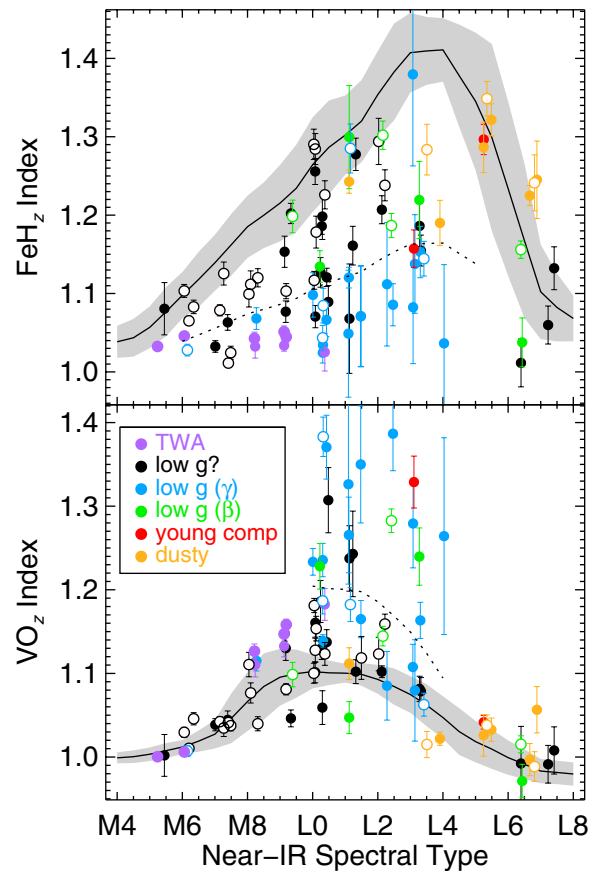
Figure 20. Gravity-sensitive indices calculated from z-band spectra. The solid black line and shaded gray region show the average and standard deviation of index values as a function of spectral type for normal field dwarfs (Burgasser et al. 2010; Cushing et al. 2005; Geißler et al. 2011; Kirkpatrick et al. 2010). Purple points represent members of the TW Hydra moving group (∼10 Myr old). Objects in our sample with an optical gravity classification of β are displayed as green points and those having an optical classification of γ are displayed as blue points (Kirkpatrick et al. 2008; Cruz et al. 2009; Rice et al. 2010b; Kirkpatrick et al. 2010). Black points show objects in our sample having no optical gravity classification. Red points represent young companions to stars. Objects having normal gravities but thought to have unusually dusty photospheres are displayed as orange points. Filled circles show index values calculated from low-resolution ($R \approx 100$) spectra, and open circles show values calculated from moderate-resolution ($R \approx 750$–2000) spectra. A gravity score of 1 is assigned to objects having an index value more than 1σ away from the field dwarf sequence. The dotted lines show the boundary for objects to be assigned a score of 2 (rather than 1).

(A color version of this figure is available in the online journal.)

dwarfs is more subtle. We do not use the other notable VO band (at ∼1.17 μm) in our analysis as this feature is blended with H_2O, FeH, and K I features.

4.2.3. Alkali Lines

Na I and K I alkali lines are the most prominent features in the J-band spectra of late-M and L field dwarfs. Pressure broadening and the condensation of opacity sources contribute to the large EWs (∼10 Å; Cushing et al. 2005) measured for these features at spectral types of L0–L6. The K I and Na I lines are blended with FeH, Fe I, and H_2O features in low-resolution spectra of late-M to mid-L dwarfs, which limits the reliability of these features as age indicators at low spectral resolution. Allers et al. (2007) established a gravity-sensitive index from the 1.14 μm Na I line, which is appropriate for $R \gtrsim 300$ spectra. We tested this index on the moderate-resolution spectra in our sample and found that

Table 5
Gravity Classifications for Low-resolution Spectra

Object	SpT		FeH$_z$	Index Values		H-cont	Gravity	Gravity
	Optical	Near-IR		VO$_z$	K I$_J$		Scores[a]	Class
2MASS J00274197+0503417	M9.5	L0	1.127 ± 0.019	1.186 ± 0.025	1.071 ± 0.015	1.010 ± 0.014	1112	INT-G
2MASS J00325584−4405058	L0.0γ	L0	1.098 ± 0.028	1.233 ± 0.016	1.077 ± 0.012	0.973 ± 0.008	2112	VL-G
2MASS J00332386−1521309	L4.0β	L1	1.300 ± 0.066	1.047 ± 0.019	1.126 ± 0.024	0.916 ± 0.010	000?	FLD-G
WISEP J004701.06+680352.1	$\cdots$	L7	1.060 ± 0.024	0.991 ± 0.023	1.026 ± 0.010	0.912 ± 0.014	nnn1	$\cdots$
2MASS J01033203+1935361	L6.0β	L6	1.038 ± 0.031	0.971 ± 0.020	0.987 ± 0.024	0.905 ± 0.018	nnn1	$\cdots$
2MASS J01174748−3403258	L2.0	L1	1.161 ± 0.025	1.243 ± 0.051	1.062 ± 0.018	0.962 ± 0.013	1121	INT-G
2MASS J01262109+1428057	L4.0γ	L2	1.112 ± 0.079	1.085 ± 0.041	1.036 ± 0.049	0.966 ± 0.028	2022	VL-G
2MASS J01415823−4633574	L0.0γ	L0	1.066 ± 0.021	1.371 ± 0.038	1.044 ± 0.022	1.003 ± 0.008	2222	VL-G
2MASS J02292794−0053282	$\cdots$	L0	1.089 ± 0.021	1.307 ± 0.039	1.055 ± 0.030	0.972 ± 0.029	2221	VL-G
2MASS J02411151−0326587	L0.0γ	L1	1.071 ± 0.064	1.350 ± 0.070	1.060 ± 0.028	0.947 ± 0.029	2221	VL-G
2MASS J03350208+2342356	M8.5	M7	1.063 ± 0.010	1.044 ± 0.011	1.050 ± 0.011	0.992 ± 0.011	1n?2	VL-G
LP 944−20	M9.0	L0	1.186 ± 0.010	1.130 ± 0.014	1.112 ± 0.012	0.948 ± 0.004	1?01	INT-G
2MASS J03552337+1133437	L5.0γ	L3	1.380 ± 0.117	1.108 ± 0.027	1.079 ± 0.027	0.939 ± 0.010	0?11	INT-G
2MASS J04062677−3812102	L0.0γ	L1	1.049 ± 0.081	1.326 ± 0.119	1.001 ± 0.057	0.958 ± 0.027	2221	VL-G
2MASS J04070752+1546457	L3.5	L3	1.155 ± 0.020	1.079 ± 0.016	1.131 ± 0.017	0.873 ± 0.006	20?0	FLD-G
2MASS J05012406−0010452	L4.0γ	L3	1.153 ± 0.033	1.163 ± 0.022	1.082 ± 0.015	0.966 ± 0.010	2112	VL-G
2MASS J05184616−2756457	L1.0γ	L1	1.120 ± 0.013	1.266 ± 0.045	1.049 ± 0.016	0.985 ± 0.011	2222	VL-G
2MASS J05341594−0631397	M8.0γ	M8	1.068 ± 0.014	1.115 ± 0.012	1.040 ± 0.019	1.000 ± 0.025	2n22	VL-G
2MASS J05361998−1920396	L2.0γ	L2	1.086 ± 0.027	1.387 ± 0.044	1.073 ± 0.018	0.991 ± 0.014	2212	VL-G
2MASS J05575096−1359503	M7.0	M7	1.032 ± 0.007	1.039 ± 0.007	1.032 ± 0.007	1.026 ± 0.008	2n22	VL-G
2MASS J06085283−2753583	M9.0γ	L0	1.034 ± 0.012	1.139 ± 0.007	1.032 ± 0.010	1.012 ± 0.011	2122	VL-G
2MASS J06195260−2903592	M6.0	M5	1.081 ± 0.033	1.002 ± 0.025	1.034 ± 0.018	1.033 ± 0.009	nnnn	$\cdots$
G 196−3B	L3.0	L3	1.157 ± 0.024	1.329 ± 0.031	1.088 ± 0.024	0.986 ± 0.010	2212	VL-G
SDSS J102552.43+321234.0	$\cdots$	L7	1.132 ± 0.027	1.008 ± 0.028	1.071 ± 0.027	0.850 ± 0.011	nnn0	$\cdots$
DENIS-P J104731.1−181558	L2.5	L0	1.198 ± 0.029	1.059 ± 0.020	1.081 ± 0.025	0.894 ± 0.007	?0?0	FLD-G
Gl 417B	L4.5	L5	1.297 ± 0.019	1.042 ± 0.008	1.120 ± 0.011	0.881 ± 0.006	0n01	FLD-G
TWA 26	M9.0	M9	1.034 ± 0.007	1.133 ± 0.013	1.030 ± 0.012	0.999 ± 0.010	2n22	VL-G
TWA 27A	M8.0	M8	1.032 ± 0.015	1.110 ± 0.014	1.030 ± 0.011	1.005 ± 0.008	2n22	VL-G
TWA 27B	$\cdots$	L3	$\cdots$	$\cdots$	1.091 ± 0.017	1.027 ± 0.008	nn12	VL-G
TWA 29	M9.5	L0	1.025 ± 0.024	1.182 ± 0.019	1.029 ± 0.011	1.002 ± 0.019	2122	VL-G
2MASS J15474719−2423493	M9.0	L0	1.121 ± 0.012	1.137 ± 0.015	1.102 ± 0.013	0.956 ± 0.009	1101	INT-G
2MASS J15515237+0941148	L4.0γ	L4	1.036 ± 0.100	1.264 ± 0.118	1.098 ± 0.026	0.992 ± 0.021	2212	VL-G
2MASS J15525906+2948485	L0.0β	L0	1.134 ± 0.020	1.228 ± 0.027	1.081 ± 0.019	0.969 ± 0.008	11?1	INT-G
2MASS J15575011−2952431	M9.0δ	L1	1.071 ± 0.064	1.165 ± 0.022	1.011 ± 0.020	0.993 ± 0.018	2122	VL-G
2MASS J16154255+4953211	L4.0γ	L3	1.138 ± 0.063	1.080 ± 0.061	1.073 ± 0.014	0.990 ± 0.007	2022	VL-G
2MASS J17054834−0516462	L0.5	L1	1.278 ± 0.021	1.102 ± 0.014	1.123 ± 0.013	0.918 ± 0.004	0001	FLD-G
2MASS J17073334+4301304	L0.5	M9	1.153 ± 0.020	1.148 ± 0.009	1.099 ± 0.032	0.926 ± 0.010	?n00	FLD-G
2MASS J17111353+2326333	L0.0	L1	1.068 ± 0.070	1.238 ± 0.039	1.084 ± 0.028	0.950 ± 0.025	2111	INT-G
2MASS J17260007+1538190	L3.0β	L3	1.219 ± 0.049	1.240 ± 0.034	1.111 ± 0.033	0.935 ± 0.010	12?1	INT-G
2MASS J17312974+2721233	L0.0	L0	1.256 ± 0.017	1.101 ± 0.013	1.122 ± 0.013	0.929 ± 0.005	0000	FLD-G
2MASS J19355595−2846343	M9.0	M9	1.077 ± 0.014	1.130 ± 0.015	1.053 ± 0.016	1.001 ± 0.009	2n12	VL-G
2MASS J20135152−2806020	M9.0	L0	1.071 ± 0.014	1.161 ± 0.017	1.053 ± 0.011	0.976 ± 0.014	2122	VL-G
2MASS J20575409−0252302	L1.5	L2	1.207 ± 0.018	1.102 ± 0.007	1.104 ± 0.017	0.907 ± 0.006	101?	INT-G
DENIS-P J220002.0−303832	L0.0	M9	1.202 ± 0.013	1.046 ± 0.010	1.093 ± 0.014	0.955 ± 0.009	0n0?	FLD-G
2MASS J22081363+2921215	L3.0γ	L3	1.082 ± 0.072	1.279 ± 0.053	1.065 ± 0.044	0.976 ± 0.018	2222	VL-G
2MASS J22134491−2136079	L0.0γ	L0	1.025 ± 0.013	1.236 ± 0.020	1.003 ± 0.015	1.018 ± 0.013	2122	VL-G
2MASS J22443167+2043433	L6.5	L6	1.011 ± 0.031	0.992 ± 0.044	0.995 ± 0.012	0.904 ± 0.013	nnn1	$\cdots$
SDSS J224953.47+004404.6AB	L3.0	L3	1.186 ± 0.029	1.081 ± 0.015	1.088 ± 0.007	0.930 ± 0.007	1011	INT-G

Note. [a] Gravity scores are listed in the following order: FeH, VO, alkali lines, and H-band continuum shape. See Section 4.3 for details.

while the index does an excellent job of distinguishing low-gravity M dwarfs from field M dwarfs, it is not as effective at determining the gravity of L dwarfs.

We have established a K I$_J$ index to measure the depth of the 1.244 and 1.253 μm K I feature at low resolution. The index is calculated using Equation (1). The index is contaminated by an FeH feature at 1.239 μm. Fortunately, the trend of FeH strength with gravity is similar to the dependence of the K I line depth with age. Figure 22 shows the K I$_J$ index, which is sensitive to gravity for spectral types of M5–L6 for low-resolution spectra.

From moderate-resolution spectra, we can calculate the pseudo-EWs of the K I and Na I lines. Table 7 and Figure 18

show the line and continuum wavelengths for our calculation of EWs. We use line windows of 0.006 μm and continuum windows of 0.002 μm (both of which are much larger than a single resolution element for $R = 750$). We approximate the continuum in the line region from a linear fit to the flux in the continuum windows, and use the rms scatter about the fit in the continuum windows as the flux uncertainty per pixel. We then propagate uncertainties using a Monte Carlo method to compute the uncertainty in the EW. We calculated EWs for the Na I lines centered at 1.1396 μm, and the K I lines centered at 1.1692, 1.1778, 1.2437, and 1.2529 μm, which are presented in Table 8 and Figures 21 and 23. We do not use the 1.2437 μm K I

Table 6
Gravity Classifications for Moderate-resolution Spectra

Object	SpT		FeH$_z$	Index Values		H-cont	Gravity	Gravity
	Optical	Near-IR		FeH$_J$	VO$_z$		Scores[a]	Class
2MASS J00034227−2822410	M7.5	M7	1.125 ± 0.015	1.100 ± 0.012	1.035 ± 0.010	0.966 ± 0.007	0n00	FLD-G
2MASS J00192626+4614078	M8.0	M8	1.120 ± 0.012	1.113 ± 0.011	1.040 ± 0.008	0.973 ± 0.005	1n11	INT-G
2MASS J00452143+1634446	L2.0β	L2	1.187 ± 0.015	1.192 ± 0.016	1.283 ± 0.014	0.942 ± 0.007	1221	VL-G
2MASS J01033203+1935361	L6.0β	L6	1.156 ± 0.011	1.098 ± 0.011	1.015 ± 0.010	0.896 ± 0.007	1n11	INT-G
SERC 296A	M6.0	M6	1.065 ± 0.006	1.062 ± 0.006	1.010 ± 0.005	0.996 ± 0.005	0n22	VL-G
2MASS J01415823−4633574	L0.0γ	L0	1.085 ± 0.022	1.122 ± 0.018	1.383 ± 0.024	1.001 ± 0.009	2212	VL-G
GSC 08047−00232B	$\cdots$	L1	$\cdots$	1.120 ± 0.055	$\cdots$	0.953 ± 0.010	2n21	VL-G
2MASSI J0253597+320637	M7.5	M6	1.083 ± 0.009	1.060 ± 0.012	1.046 ± 0.007	0.972 ± 0.004	0n00	FLD-G
2MASS J03140344+1603056	L0.0	L0	1.284 ± 0.020	1.221 ± 0.014	1.128 ± 0.014	0.912 ± 0.007	0?00	FLD-G
2MASS J03350208+2342356	M8.5	M7	1.079 ± 0.007	1.077 ± 0.006	1.042 ± 0.006	0.991 ± 0.004	1n22	VL-G
LP 944−20	M9.0	L0	1.226 ± 0.018	1.212 ± 0.018	1.123 ± 0.014	0.946 ± 0.008	0?01	FLD-G
2MASS J03552337+1133437	L5.0γ	L3	1.144 ± 0.022	1.106 ± 0.012	1.063 ± 0.014	0.971 ± 0.005	2022	VL-G
2MASS J04221413+1530525	M6.0γ	M6	1.028 ± 0.007	1.018 ± 0.006	1.007 ± 0.007	0.996 ± 0.004	2n22	VL-G
2MASS J04351455−1414468	M7.0	M7	1.024 ± 0.008	1.021 ± 0.005	1.038 ± 0.006	1.031 ± 0.004	2n22	VL-G
2MASS J04362788−4114465	M8.0	M9	1.103 ± 0.010	1.112 ± 0.008	1.081 ± 0.007	0.986 ± 0.006	1n22	VL-G
2MASS J04433761+0002051	M9.5	L0	1.117 ± 0.011	1.148 ± 0.010	1.181 ± 0.009	0.973 ± 0.005	1122	VL-G
2MASS J05575096−1359503	M7.0	M7	1.011 ± 0.005	1.023 ± 0.005	1.041 ± 0.007	1.018 ± 0.005	2n22	VL-G
2MASS J06023045+3910592	L1.0	L2	1.238 ± 0.020	1.223 ± 0.012	1.159 ± 0.012	0.910 ± 0.007	111?	INT-G
2MASS J06085283−2753583	M9.0γ	L0	1.043 ± 0.016	1.081 ± 0.012	1.187 ± 0.015	0.983 ± 0.007	2122	VL-G
CD−35 2722B	$\cdots$	L3	$\cdots$	1.243 ± 0.034	$\cdots$	$\cdots$	1n1n	INT-G
AB PicB	$\cdots$	L0	$\cdots$	1.104 ± 0.015	$\cdots$	0.985 ± 0.008	2n22	VL-G
LP 423−31	M7.0	M6	1.103 ± 0.008	1.078 ± 0.009	1.029 ± 0.006	0.972 ± 0.005	0n00	FLD-G
2MASS J08040580+6153336	M9.0	M8	1.099 ± 0.017	1.124 ± 0.020	1.111 ± 0.015	0.935 ± 0.006	1n00	FLD-G
G 196−3B	L3.0	L3	$\cdots$	1.231 ± 0.029	$\cdots$	0.961 ± 0.015	1n22	VL-G
2MASS J10220489+0200477	M9.0β	M9	1.198 ± 0.021	1.196 ± 0.023	1.099 ± 0.015	0.940 ± 0.008	0n00	FLD-G
2MASS J10224821+5825453	L1.0γ	L1	1.285 ± 0.031	1.228 ± 0.024	1.182 ± 0.020	0.913 ± 0.008	1100	FLD-G
2MASS J10452400−0149576	L1.0	L1	$\cdots$	1.250 ± 0.024	1.119 ± 0.026	0.901 ± 0.009	??10	FLD-G
TWA 28	M8.5	M9	1.045 ± 0.008	1.081 ± 0.010	1.158 ± 0.007	1.011 ± 0.006	2n22	VL-G
TWA 5B	$\cdots$	M9	$\cdots$	1.067 ± 0.011	$\cdots$	0.988 ± 0.007	2n22	VL-G
TWA 8B	M5.0	M6	1.046 ± 0.004	1.043 ± 0.004	1.006 ± 0.004	0.998 ± 0.005	1n22	VL-G
TWA 26	M9.0	M9	1.051 ± 0.007	1.069 ± 0.006	1.147 ± 0.006	0.995 ± 0.005	2n22	VL-G
TWA 27A	M8.0	M8	1.043 ± 0.008	1.070 ± 0.011	1.126 ± 0.009	1.002 ± 0.006	2n22	VL-G
TWA 11C	M4.5	M5	1.032 ± 0.005	1.028 ± 0.006	1.000 ± 0.004	0.996 ± 0.004	nn2n	VL-G
2MASS J14112131−2119503	M9.0	M8	1.112 ± 0.017	1.120 ± 0.014	1.077 ± 0.012	0.961 ± 0.006	1n10	INT-G
2MASS J15474719−2423493	M9.0	L0	1.178 ± 0.020	1.155 ± 0.018	1.154 ± 0.015	0.963 ± 0.008	1111	INT-G
2MASS J17260007+1538190	L3.0β	L3	$\cdots$	1.206 ± 0.021	$\cdots$	$\cdots$	1n1n	INT-G
2MASS J17312974+2721233	L0.0	L0	1.290 ± 0.019	1.215 ± 0.014	1.100 ± 0.012	0.917 ± 0.006	0000	FLD-G
2MASS J19355595−2846343	M9.0	M9	$\cdots$	1.101 ± 0.022	$\cdots$	0.986 ± 0.011	1n12	INT-G
2MASS J20575409−0252302	L1.5	L2	1.294 ± 0.029	1.285 ± 0.025	1.123 ± 0.020	0.891 ± 0.008	??10	FLD-G
2MASS J22443167+2043433	L6.5	L6	$\cdots$	1.020 ± 0.010	$\cdots$	0.909 ± 0.006	2n21	VL-G
2MASS J23224684−3133231	L0.0β	L2	1.302 ± 0.018	1.200 ± 0.016	1.145 ± 0.012	0.928 ± 0.007	1101	INT-G

Notes. [a] Gravity scores are listed in the following order: FeH, VO, alkali lines, and H-band continuum shape. See Section 4.3 for details.

EW in our youth analysis, as it is blended with an FeH feature, which results in large uncertainties (see Figure 23). The J-band Na I and K I EWs show similar dependence on spectral type and gravity, with TWA members having substantially weaker absorption than field dwarfs.

4.2.4. H-band Continuum Shape

A hallmark of youth seen in the near-IR spectra of late-M and L dwarfs at low spectral resolution is a triangular H-band continuum shape (Figure 10). Though both very low and intermediate-gravity objects have a triangular shape compared to field dwarfs, intermediate-gravity objects appear to have a "shoulder" at $\sim$1.57 μm, likely due to a combination of increased FeH absorption and H_2 collision induced absorption (Borysow et al. 1997). As noted by Bowler et al. (2012), the H-band continuum shape for intermediate-age ($\sim$50–150 Myr) M9 dwarfs is less triangular than that of a $\sim$12 Myr old TWA M9

Table 7
Line Equivalent Width Calculation[a]

Species	λ_{line} (μm)	λ_{cont1} (μm)	λ_{cont2} (μm)	Window$_{line}$ (μm)	Window$_{cont}$ (μm)
Na I	1.1396	1.1310	1.1470	0.006	0.002
K I	1.1692	1.1630	1.1860	0.006	0.002
K I	1.1778	1.1630	1.1860	0.006	0.002
K I	1.2437	1.2480	1.2570	0.006	0.002
K I	1.2529	1.2480	1.2570	0.006	0.002

Note. [a] The method for calculating equivalent widths is described in Section 4.2.3.

dwarf. We note that the K-band continuum shape also appears to be sensitive to gravity (Figures 10 and 11), with low-gravity objects having slightly more positive 2.15–2.25 μm spectral slopes than field dwarfs. The differences in K-band spectral
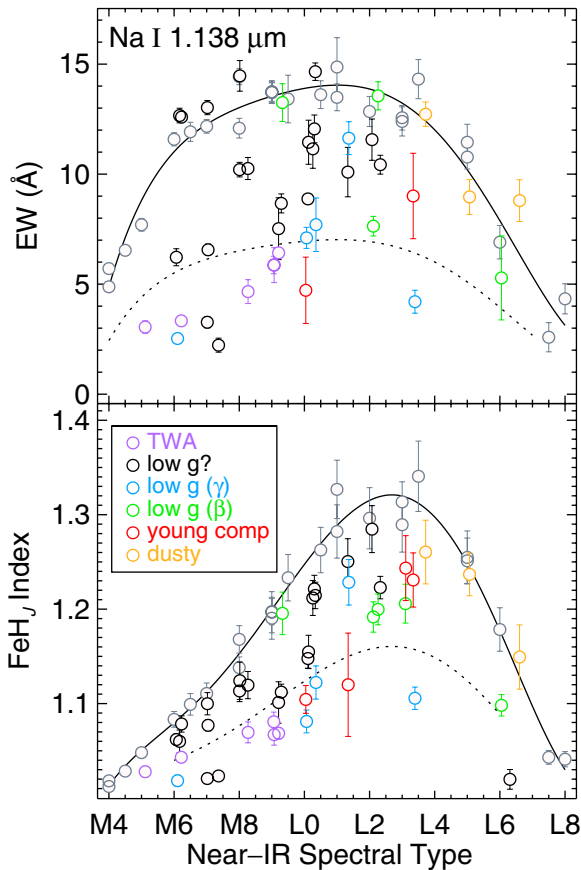
Figure 21. Na I (top) and line EWs and *J*-FeH indices measured from moderate-resolution spectra. Symbols are the same as those used in Figure 20. Gray circles show our calculated EWs for normal field dwarfs (Cushing et al. 2005).
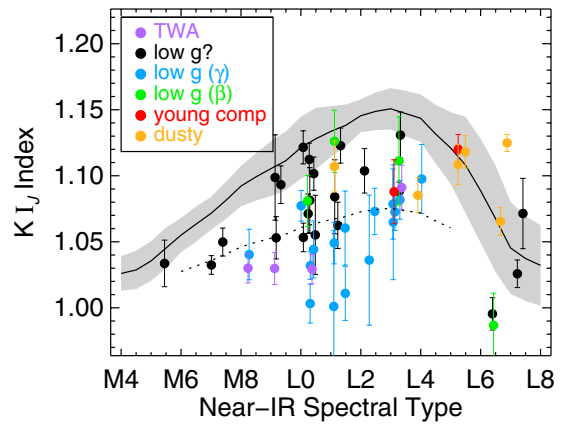
(A color version of this figure is available in the online journal.)

Figure 22. Gravity-sensitive index used to measure the depth of the 1.25 μm K I doublet. Symbols are the same as those used in Figure 20.

(A color version of this figure is available in the online journal.)

shape with gravity, however, are subtle, and dusty objects have *K*-band continuum shapes that are similar to young objects (Figure 15), so we do not use *K*-band continuum shape in our analysis.

We establish the *H*-cont index to measure the triangular shape of the *H*-band spectrum (Table 4 and Figure 19). Though calculated using Equation (1), the *H*-cont index does not measure the depth of an absorption feature, but rather measures how much the shape of the blue end of the *H*-band deviates from a straight line. For very low gravity objects the blue side of the *H* band is nearly a straight line, corresponding to an *H*-cont index value of ~1.0. Higher gravity objects have lower *H*-cont indices. The *H*-cont index is sensitive to gravity for spectral types of M6–L7. Spectra for objects earlier than M6 tend to have a fairly flat *H*-band continuum shape, so the index loses its efficacy for early- to mid-M dwarfs. The *H*-cont indices for our sample are displayed in Figure 24. Though objects classified as low gravity in the optical (γ and β) appear to have low gravity using the *H*-cont index, older "dusty" field dwarfs also show a hint of low gravity in this index (e.g., Figure 15). *Thus the continuum shape of the H band is not the most reliable gravity indicator, particularly for intermediate gravities, and should be used in combination with other gravity-sensitive features.*

4.3. A Quantitative Near-IR Gravity Classification Scheme

Having created a set of gravity-sensitive indices, our goal is to utilize the indices to quantitatively classify the gravities of objects in our sample. An optical gravity classification scheme

has been developed for L dwarfs (Cruz et al. 2009). Our near-IR gravity classification is designed to provide classifications that are consistent with the established optical classification system.

For each index and EW we determine if the value of the index indicates low gravity by comparison to the behavior seen in field dwarfs as a function of SpT. For the FeH_z, VO_z, $K I_J$ and *H*-cont indices to indicate low gravity (a score of 1), the index value for an object must lie more than 1σ from the scatter in the field dwarf sequence at the object's near-IR spectral type (i.e., the object's index and error bars must lie outside of the gray-shaded regions in Figures 20, 22, and 24). For the FeH_J index and K I and Na I EWs, we do not have a large enough sample of field objects observed at moderate spectral resolution to calculate the field sequence and its uncertainty as for the lower resolution indices. Instead, we fit a fourth-order polynomial to the measured indices/EWs of the field dwarf spectra and use the scatter about the fit as the uncertainty. The necessary index values for an object to be considered low gravity are presented in Tables 9 and 10. For each index and EW, we also create a dividing line (displayed as dashed lines in Figures 20–24) which delineates a strong indication of low gravity (a score of 2). For EWs, the dividing lines were chosen to be 50% of the field dwarf sequence. For indices, dividing lines were set to delineate feature strengths that are a fraction, α, of the features in the field dwarf sequence. The dividing lines are calculated as ((field sequence $- 1) * \alpha + 1$), where α is a scale factor chosen so that the dividing line roughly separates objects having optical classifications of β and γ.

We determine a gravity score for each of four indicators: FeH, VO, alkali lines, and *H*-band continuum shape. Following the same order, the scores are presented in Tables 5 and 6. For the low-resolution spectra in our sample, we use the following approach to assigning scores.

1. The gravity scores for FeH, VO, alkali line depth, and *H*-band continuum are taken from the scores of the FeH_z, VO_z, $K I_J$, and *H*-cont indices, respectively (Table 5).
2. A score of 0 is given if an object's index or EW is consistent with the field dwarf sequence.
3. A score of 1 means the index indicates low gravity, with the index lying at least 1σ away from the field dwarf index and uncertainty.
4. A score of 2 means the index strongly indicates low gravity and is farther from the field dwarf sequence than the dashed lines in Figures 20–24.

Table 8
Equivalent Widths Calculated from Moderate-resolution Spectra

Object	SpT		Na I 1.138 μm	K I 1.169 μm	K I 1.177 μm	K I 1.253 μm
	Optical	Near-IR	EW (Å)	EW (Å)	EW (Å)	EW (Å)
2MASS J00034227−2822410	M7.5	M7	13.02 ± 0.32	3.06 ± 0.63	6.02 ± 0.63	4.65 ± 0.50
2MASS J00192626+4614078	M8.0	M8	10.20 ± 0.33	3.44 ± 0.42	4.87 ± 0.44	3.65 ± 0.34
2MASS J00452143+1634446	L2.0β	L2	7.63 ± 0.45	4.84 ± 0.46	5.86 ± 0.46	3.90 ± 0.38
2MASS J01033203+1935361	L6.0β	L6	5.28 ± 1.91	6.39 ± 0.56	6.50 ± 0.53	5.75 ± 0.27
SERC 296A	M6.0	M6	6.22 ± 0.39	1.37 ± 0.26	2.49 ± 0.27	1.63 ± 0.21
2MASS J01415823−4633574	L0.0γ	L0	7.70 ± 1.22	3.77 ± 1.02	5.28 ± 1.05	1.92 ± 0.66
GSC 08047−00232B	· · ·	L1	· · ·	1.75 ± 2.16	2.63 ± 2.17	1.76 ± 1.32
2MASSI J0253597+320637	M7.5	M6	12.66 ± 0.33	3.58 ± 0.31	5.32 ± 0.29	2.78 ± 0.49
2MASS J03140344+1603056	L0.0	L0	12.06 ± 0.63	7.51 ± 0.31	9.35 ± 0.31	6.71 ± 0.34
2MASS J03350208+2342356	M8.5	M7	6.56 ± 0.26	1.81 ± 0.17	2.95 ± 0.17	1.93 ± 0.19
LP 944−20	M9.0	L0	11.15 ± 0.88	6.56 ± 0.80	8.54 ± 0.82	5.94 ± 0.54
2MASS J03552337+1133437	L5.0γ	L3	4.20 ± 0.52	4.43 ± 0.36	5.63 ± 0.36	3.66 ± 0.47
2MASS J04221413+1530525	M6.0γ	M6	2.53 ± 0.23	0.40 ± 0.15	0.93 ± 0.15	0.38 ± 0.21
2MASS J04351455−1414468	M7.0	M7	3.27 ± 0.26	0.75 ± 0.22	1.63 ± 0.22	0.28 ± 0.21
2MASS J04362788−4114465	M8.0	M9	8.67 ± 0.43	2.52 ± 0.37	3.99 ± 0.35	2.50 ± 0.27
2MASS J04433761+0002051	M9.5	L0	8.87 ± 0.24	3.54 ± 0.26	5.53 ± 0.26	2.83 ± 0.22
2MASS J05575096−1359503	M7.0	M7	2.23 ± 0.32	0.62 ± 0.40	1.12 ± 0.41	0.65 ± 0.26
2MASS J06023045+3910592	L1.0	L2	10.43 ± 0.43	6.35 ± 0.45	8.38 ± 0.46	5.52 ± 0.34
2MASS J06085283−2753583	M9.0γ	L0	7.10 ± 0.48	2.93 ± 0.61	4.77 ± 0.57	1.49 ± 0.42
CD−35 2722B	· · ·	L3	· · ·	7.76 ± 1.07	9.82 ± 1.09	5.67 ± 0.60
AB PicB	· · ·	L0	4.72 ± 1.51	2.83 ± 1.04	3.37 ± 1.07	1.85 ± 0.60
LP 423−31	M7.0	M6	12.59 ± 0.23	2.93 ± 0.40	4.99 ± 0.40	3.19 ± 0.26
2MASS J08040580+6153336	M9.0	M8	14.47 ± 0.70	5.36 ± 0.39	7.74 ± 0.40	5.00 ± 0.48
G 196−3B	L3.0	L3	9.01 ± 1.94	3.25 ± 0.79	5.55 ± 0.82	1.17 ± 1.32
2MASS J10220489+0200477	M9.0β	M9	13.25 ± 0.86	6.11 ± 0.79	9.00 ± 0.82	6.50 ± 0.45
2MASS J10224821+5825453	L1.0γ	L1	11.63 ± 0.75	8.22 ± 1.00	10.74 ± 0.93	6.98 ± 0.31
2MASS J10452400−0149576	L1.0	L1	10.09 ± 1.12	9.61 ± 0.76	8.42 ± 0.71	7.48 ± 1.02
TWA 28	M8.5	M9	5.87 ± 0.40	1.45 ± 0.40	2.57 ± 0.38	0.64 ± 0.38
TWA 5B	· · ·	M9	5.86 ± 0.79	0.93 ± 0.61	2.28 ± 0.57	1.43 ± 0.39
TWA 8B	M5.0	M6	3.33 ± 0.17	0.77 ± 0.27	1.60 ± 0.28	0.84 ± 0.15
TWA 26	M9.0	M9	6.42 ± 0.24	1.04 ± 0.32	2.16 ± 0.33	1.35 ± 0.18
TWA 27A	M8.0	M8	4.66 ± 0.54	1.72 ± 0.45	1.71 ± 0.43	0.92 ± 0.37
TWA 11C	M4.5	M5	3.05 ± 0.29	−0.00 ± 0.23	1.32 ± 0.23	0.72 ± 0.22
2MASS J14112131−2119503	M9.0	M8	10.26 ± 0.50	3.34 ± 0.56	5.54 ± 0.56	4.58 ± 0.36
2MASS J15474719−2423493	M9.0	L0	11.45 ± 1.00	4.91 ± 0.44	5.81 ± 0.46	5.16 ± 0.55
2MASS J17260007+1538190	L3.0β	L3	· · ·	5.92 ± 0.67	6.97 ± 0.71	4.68 ± 0.38
2MASS J17312974+2721233	L0.0	L0	14.66 ± 0.40	8.14 ± 0.22	10.29 ± 0.20	6.73 ± 0.32
2MASS J19355595−2846343	M9.0	M9	7.52 ± 1.41	3.38 ± 0.70	4.97 ± 0.72	0.84 ± 0.45
2MASS J20575409−0252302	L1.5	L2	11.57 ± 0.94	7.97 ± 0.68	10.81 ± 0.70	7.35 ± 0.54
2MASS J22443167+2043433	L6.5	L6	· · ·	4.09 ± 1.14	4.91 ± 1.08	2.82 ± 0.28
2MASS J23224684−3133231	L0.0β	L2	13.56 ± 0.64	10.18 ± 0.41	11.68 ± 0.38	8.39 ± 0.37

Table 9
Determination of Gravity Scores from Indices

SpT	FeH$_z$		FeH$_J$		VO$_z$		K I$_J$		H-cont	
Near-IR	1	2	1	2	1	2	1	2	1	2
M5	· · ·	· · ·	· · ·	· · ·	· · ·	· · ·	· · ·	· · ·	· · ·	· · ·
M6	⩽1.068	⩽1.039	⩽1.049	⩽1.040	· · ·	· · ·	⩽1.042	⩽1.028	⩾0.988	⩾0.994
M7	⩽1.103	⩽1.056	⩽1.079	⩽1.056	· · ·	· · ·	⩽1.059	⩽1.036	⩾0.981	⩾0.990
M8	⩽1.146	⩽1.074	⩽1.116	⩽1.076	· · ·	· · ·	⩽1.077	⩽1.046	⩾0.963	⩾0.984
M9	⩽1.167	⩽1.086	⩽1.160	⩽1.100	· · ·	· · ·	⩽1.085	⩽1.053	⩾0.949	⩾0.979
L0	⩽1.204	⩽1.106	⩽1.208	⩽1.124	⩾1.122	⩾1.256	⩽1.098	⩽1.061	⩾0.935	⩾0.972
L1	⩽1.252	⩽1.121	⩽1.253	⩽1.144	⩾1.112	⩾1.251	⩽1.114	⩽1.067	⩾0.914	⩾0.968
L2	⩽1.298	⩽1.142	⩽1.288	⩽1.158	⩾1.110	⩾1.232	⩽1.133	⩽1.073	⩾0.906	⩾0.964
L3	⩽1.357	⩽1.163	⩽1.296	⩽1.160	⩾1.097	⩾1.187	⩽1.135	⩽1.075	⩾0.898	⩾0.960
L4	⩽1.370	⩽1.164	⩽1.260	⩽1.149	⩾1.073	⩾1.118	⩽1.126	⩽1.072	⩾0.885	⩾0.954
L5	⩽1.258	⩽1.138	⩽1.199	⩽1.124	· · ·	· · ·	⩽1.094	⩽1.061	⩾0.869	⩾0.949
L6	· · ·	· · ·	⩽1.121	⩽1.089	· · ·	· · ·	· · ·	· · ·	⩾0.874	⩾0.950
L7	· · ·	· · ·	· · ·	· · ·	· · ·	· · ·	· · ·	· · ·	⩾0.888	⩾0.952
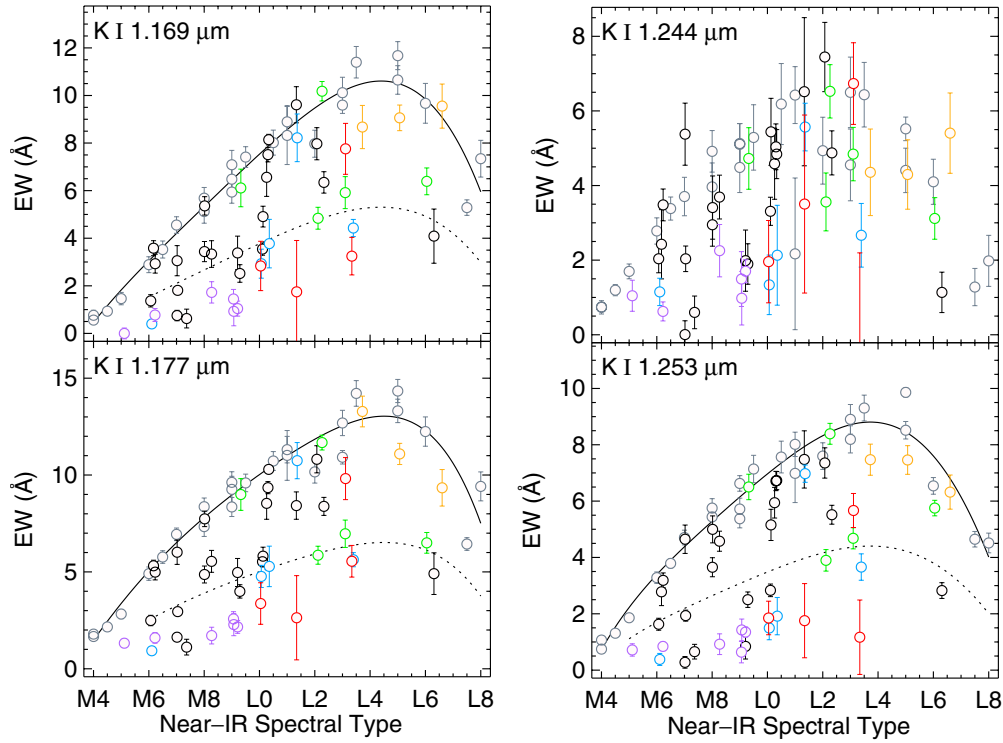
Figure 23. K I equivalent widths measured from moderate-resolution spectra. Symbols are the same as those used in Figure 20. Gray circles show the EWs calculated for normal field dwarfs from Cushing et al. (2005).

(A color version of this figure is available in the online journal.)

Table 10
Determination of Gravity Scores from Equivalent Widths

SpT Near-IR	N I 1.138 μm EW (Å)		K I 1.169 μm EW (Å)		K I 1.177 μm EW (Å)		K I 1.253 μm EW (Å)	
	1	2	1	2	1	2	1	2
M5	⩽6.128	⩽4.402	⋯	⋯	⋯	⋯	⩽0.905	⩽1.112
M6	⩽9.087	⩽5.509	⩽1.632	⩽1.524	⩽3.124	⩽2.521	⩽2.215	⩽1.696
M7	⩽10.742	⩽6.132	⩽2.816	⩽2.102	⩽4.690	⩽3.255	⩽3.277	⩽2.190
M8	⩽11.700	⩽6.511	⩽3.954	⩽2.665	⩽6.067	⩽3.903	⩽4.214	⩽2.642
M9	⩽12.318	⩽6.770	⩽5.074	⩽3.222	⩽7.290	⩽4.483	⩽5.094	⩽3.072
L0	⩽12.754	⩽6.948	⩽6.179	⩽3.767	⩽8.396	⩽5.012	⩽5.937	⩽3.483
L1	⩽13.018	⩽7.022	⩽7.244	⩽4.282	⩽9.408	⩽5.495	⩽6.727	⩽3.856
L2	⩽12.629	⩽6.934	⩽8.223	⩽4.736	⩽10.325	⩽5.924	⩽7.414	⩽4.161
L3	⩽11.712	⩽6.614	⩽9.042	⩽5.089	⩽11.113	⩽6.273	⩽7.926	⩽4.356
L4	⩽10.194	⩽6.007	⩽9.605	⩽5.284	⩽11.693	⩽6.487	⩽8.056	⩽4.395
L5	⩽8.107	⩽5.099	⩽9.450	⩽5.255	⩽11.619	⩽6.484	⩽7.473	⩽4.227
L6	⩽5.635	⩽3.942	⩽8.417	⩽4.923	⩽10.483	⩽6.142	⩽6.331	⩽3.801
L7	⩽3.175	⩽2.677	⩽6.496	⩽4.197	⩽8.154	⩽5.302	⩽4.545	⩽3.073

5. Scores of "?" are given if an index hints at low gravity, but the uncertainty in the calculated index is too large (i.e., the index lies outside of the gray shaded regions shown in Figures 20–24, but the error bars overlap).

6. Scores of "n" are assigned if either the spectrum does not fully cover the wavelength range of the index or the index is not gravity-sensitive for the object's spectral type.

For our moderate-resolution spectra, we determine the gravity scores in a similar manner as for low-resolution spectra, but include the measurements for the FeH$_J$ index and the Na I and K I EWs when determining the gravity scores. Here is the approach.

1. The gravity scores for VO and H-band continuum are taken from the scores of the VO$_z$ and H-cont indices, respectively.

2. The gravity score for FeH is assigned based on the FeH$_z$ and FeH$_J$ index scores. If either of the FeH$_z$ and FeH$_J$ index scores is 1, an FeH gravity score of 1 is assigned. If either index has a score of 2, an FeH gravity score of 2 is assigned.

3. The gravity score for alkali lines is assigned based on the Na I and three K I line EWs. We determine the alkali line score from the mean of the individual line EW scores rounded to the nearest integer.

For a given object, the scores for the individual absorption species are usually in reasonable but not exact agreement, reflecting the underlying scatter in the strengths of these features as a function of spectral type. It is valuable to be able to describe the overall low-gravity nature of a source, analogous to the

19
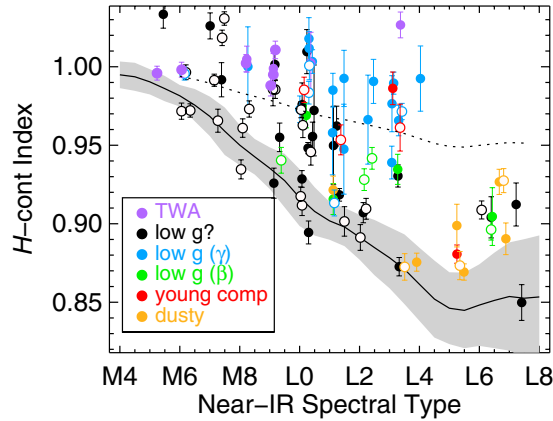
Figure 24. Gravity-sensitive index measuring the continuum shape of the *H* band. Symbols are the same as those used in Figure 20.

(A color version of this figure is available in the online journal.)

overall spectral morphology that is represented by the spectral type, even though there can be small spectral differences.

Desiring an objective and automatic approach, we determine an overall gravity classification from the median of the object's gravity scores. Gravity scores of n and ? are ignored for the purposes of computing the median. When there are an even number of scores, we take the average of the two values straddling the median, e.g., "0101" gives an overall score of 0.5. With the resulting medians, we define three near-IR gravity classifications.

1. FLD-G: the object has gravity scores consistent with normal field dwarfs. The median gravity score is $\leqslant 0.5$.
2. INT-G: the object has gravity scores consistent with intermediate gravity. The median gravity score is 1.

3. VL-G: the object has gravity scores consistent with very low gravity. The median gravity score is $\geqslant 1.5$.

The near-IR gravity classifications of our sample are presented in Table 5. The Appendix gives examples of gravity classifications using our method. Figure 25 presents a sequence of VL-G objects with spectral types of M5–L6.

Thirty of the near-IR spectra in our sample have gravity classifications (β, γ, or δ) determined from optical spectra (Cruz et al. 2009; Kirkpatrick et al. 2010; Rice et al. 2010b; Faherty et al. 2013), where β implies intermediate gravity and γ and δ imply very low gravity. Of the 21 spectra in our sample of objects having an optical classification of γ or δ, we classify 19 as VL-G, 1 as INT-G (the prism spectrum of 2M 0355+11), and 1 (2M 1022+58) as FLD-G in the near-IR. Thus, sources characterized as very low gravity in the optical usually have very low gravity spectral features in near-IR as well. Objects having optical gravity classifications of β are generally classified as INT-G (six/nine objects). One optically classified β object, 2M 0045+16, is classified as VL-G in the near-IR. Two sources, 2M 0033−15 and 2M 1022+02, having optical gravity classifications of β, show no signs of youth in any of the indicators and are classified as FLD-G. Overall, our near-IR classification system produces gravity classifications consistent with the optical system of Cruz et al. (2009).

Our sample includes 16 young sources for which we have both low-resolution and moderate-resolution spectra. Our gravity classifications from both low and moderate resolution agree for all but four of these sources (LP 944−20, 2M 0355+11, 2M 2057−02, and 2M 1935−28). For LP 944−20, both the low- and moderate-resolution spectra indicate low gravity in the H-cont index and hint at low gravity in the VO_z index (scores of "?"). From its moderate-resolution spectrum, the Na I EW of LP 944−20 also indicates low gravity (score of 1). The FeH_z
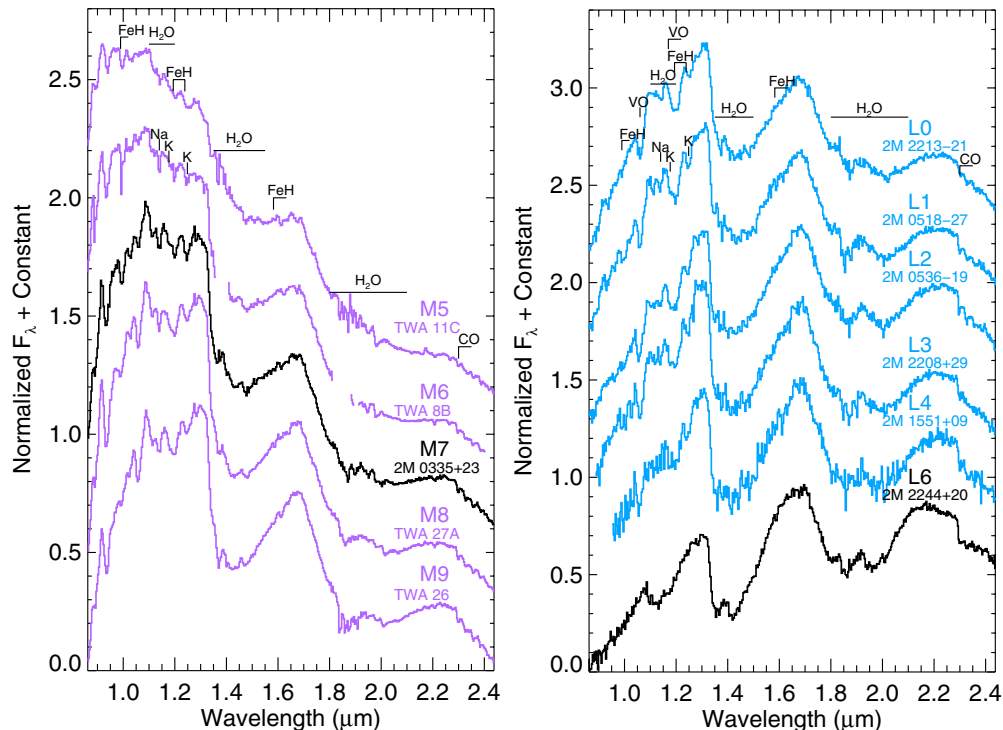
Figure 25. Our sequence of field dwarfs classified as having very low gravity (VL-G) in the near-IR. Spectra plotted in purple are for known members of TWA. Spectra plotted in blue are of objects having optical gravity classifications of γ. Objects plotted in black have no available optical gravity classification.

(A color version of this figure is available in the online journal.)

and FeH$_J$ indices as well as the K I EWs of LP 944−20 are lower than the field sequence, but are not quite low enough to result in index scores of 1. Thus, LP 944−20 is a good example of a source that is on the borderline between being classified as INT-G or FLD-G. For 2M 2057−02, its low- and moderate-resolution spectra result in classifications of INT-G and FLD-G, respectively. The gravity scores from its moderate-resolution spectrum are ??10. Like LP 944−20, 2M 2057−02 is also a good example of a borderline source. For 2M 1935−28, its low- and moderate-resolution spectra result in classifications VL-G and INT-G, respectively. Both the low- and moderate-resolution spectra of 2M 1935−28 receive an alkali line score of 1 and an H-band continuum score of 2. The difference in the gravity classifications for the two different resolutions lies in the FeH indicator. For the low-resolution spectrum, the FeH gravity score (1) comes from the FeH$_z$ index, whereas in the moderate-resolution spectrum the FeH gravity score (2) is assigned from the FeH$_J$ index. For 2M 0355+11, both the moderate- and low-resolution spectra indicate low gravity, but with classifications of VL-G and INT-G, respectively. The low-resolution spectrum of 2M 0355+11 is fairly noisy in the z-band (S/N ∼ 10), as reflected in the high uncertainty in the FeH$_z$ index. The K I$_J$ and H-cont indices, as calculated from the low-resolution spectrum of 2M 0355+11, clearly indicate low gravity but do not meet the criteria for index scores of 2. Given the higher signal-to-noise ratio (S/N) for indices and EWs measured from moderate-resolution spectra, we adopt the classifications based on moderate-resolution spectra where available. In general, there is good agreement between gravity determinations using low-resolution and moderate-resolution spectra, which highlights the effectiveness of our indices.

We included published spectra of dusty objects (Kirkpatrick et al. 2010; Looper et al. 2008) to test if our gravity classification system correctly classifies these peculiar objects as having normal (field) gravity. These dusty objects are plotted in Figures 20–24 as orange points. As noted above, several of the dusty objects appear to be low gravity in the H-cont index. Despite this, we classify all of the dusty objects as FLD-G when considering all of their gravity-sensitive index values. Our index-based gravity classification can thus be used to discriminate between low-gravity and dusty objects.

4.4. Proposed Low-gravity Spectral Standards

The near-IR spectra of low-gravity objects can show remarkable variation in near-IR colors as well as spectral features, as shown in Figure 8. Our method of spectral type and gravity classification described above will determine reliable spectral types and gravities, without bias to near-IR color or preconceived ideas of gravity. A great deal of current work relies on the use of spectral templates for determination of spectral types, particularly for optical spectroscopy (e.g., West et al. 2011). There does not currently exist a set of near-IR spectral templates for low-gravity ultracool dwarfs. Having determined the spectral types and gravities for our sample, we propose a set of VL-G spectral standards. We note that these standards can be used as spectral templates, but recommend comparison to individual features, as determining best-fit templates to the entire 0.8–2.5 μm spectrum can often be biased toward fitting the closest near-IR color. We selected possible spectral standards using the following criteria.

1. Proposed low-gravity standards should have near-IR spectral types that are identical or similar to their optical spectral types. This assures that an object classified using our pro-
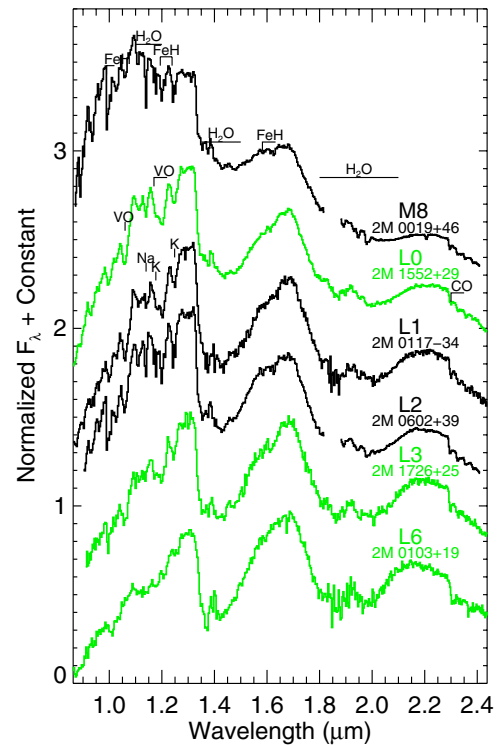
Figure 26. A sequence of field dwarfs classified as having intermediate gravity (INT-G) in the near-IR. Spectra plotted in green are for objects with optical gravity classifications of β. Objects plotted in black have no available optical gravity classification.

(A color version of this figure is available in the online journal.)

posed near-IR spectral standards will, in general, have a similar optical spectral classification.
2. Standard spectra should show a strong indication of low gravity (a score of 2) in the majority of our gravity-sensitive indices. Our proposed standards have firm VL-G classifications.
3. Preference is given to objects that are known members of young kinematic groups (see Section 4.5.1) or have optical gravity classifications of γ, as this additional information helps to more fully understand their properties.
4. Preference is given to objects that have high-S/N spectra, to allow for easy comparison to future work.

Figure 25 presents a proposed sequence of VL-G spectral standards. Our proposed spectral standards show a smooth progression of spectral features in the J, H, and K windows, as well as an overall trend toward redder $J − K$ colors at later spectral types. We note that no L5-type object met the criteria listed above, so this subtype is lacking in our sequence.

In general, we find that objects classified as INT-G show more variation in their gravity-sensitive features at a given spectral type than objects classified as VL-G. Our sample also consists of fewer INT-G objects than VL-G objects. Thus, determining a full sequence of INT-G standards would be premature at this time. Figure 26 shows spectra for objects that meet the criteria to be INT-G standards. Spectral types of M5–M7, M9, and L4–L5 are not represented, as suitable standards are not available in our sample.

4.5. The Ages of Low-gravity Ultracool Dwarfs

Determining how our gravity classifications correspond to a specific age is difficult. In addition, the age sensitivity of

Table 11
Young Field Objects with Age Estimates

Object	SpT Near-IR	Gravity Near-IR	Age (Myr)	Notes	Ref.
TWA 28	M9	VL-G	∼10	TWA member	S05
TWA 5B	M9	VL-G	∼10	TWA member	W99
TWA 8B	M6	VL-G	∼10	TWA member	W99
TWA 26	M9	VL-G	∼10	TWA member	G02
TWA 27A	M8	VL-G	∼10	TWA member	G02
TWA 27B	L3	VL-G	∼10	TWA member	Ch04
TWA 11C	M5	VL-G	∼10	TWA member	Ka08, W13
TWA 29	L0	VL-G	∼10	TWA member	L07, W13
2MASS J03350208+2342356	M7	VL-G	≲10	Li	S09
2MASS J05575096−1359503	M7	VL-G	≲10	Li	S09
2MASS J06085283−2753583	L0	VL-G	∼10?	βPic candidate	R10
GSC 08047−00232B	L1	VL-G	∼30	Tuc–Hor member	Ch05a
AB Pic B	L0	VL-G	∼30	Tuc–Hor member	Ch05b
2MASS J01415823−4633574	L0	VL-G	∼30?	Tuc–Hor candidate	K06
G 196−3B	L3	VL-G	20-300	Age for G 196−3A	R98, K01
2MASS J03552337+1133437	L3	VL-G	∼100	AB Dor member	L13
CD−35 2722B	L3	INT-G	∼100	AB Dor member	W11
2MASS J06023045+3910592	L2	INT-G	∼100?	Pleiades candidate	S10
LP 944−20	L0	FLD-G	∼200?	Castor candidate	R03
Gl 417B	L5	FLD-G	80-300, 750	Age for Gl 417A	K01, A10
SERC 296A	M6	VL-G	≲200	Li	T97
2MASS J00192626+4614078	M8	INT-G	≲300	Li	R09
2MASS J14112131−2119503	M8	INT-G	≲300	Li	R09
2MASS J03140344+1603056	L0	FLD-G	∼500?	UMaj candidate	S10
2MASS J17054834−0516462	L1	FLD-G	∼500?	UMaj candidate	S10

References. A10: Allers et al. 2010; Ch04: Chauvin et al. 2004; Ch05a: Chauvin et al. 2005a; Ch05b: Chauvin et al. 2005b; G02: Gizis 2002; K01: Kirkpatrick et al. 2001; K06: Kirkpatrick et al. 2006; Ka08: Kastner et al. 2008; L13: Liu et al. 2013; L07: Looper et al. 2007; R98: Rebolo et al. 1998; R09: Reiners & Basri 2009; R10: Rice et al. 2010b; S03: Salim et al. 2003; S05: Scholz et al. 2005; S09: Shkolnik et al. 2009; S10: Seifahrt et al. 2010; S12: Shkolnik et al. 2012; T97: Thackrah et al. 1997; W99: Webb et al. 1999; W11: Wahhaj et al. 2011; W13: Weinberger et al. 2013.

our indices could be dependent on spectral type. As shown in the previous section, our near-IR gravity classifications of VL-G and INT-G are consistent with optical classifications of γ and β, respectively. Based on analysis of gravity-sensitive features in optical spectra, Cruz et al. (2009) estimate the ages for γ and β classifications to be log(age (yr)) ≈ 7 and log(age yr)) ≈ 8. We can examine age estimates for a number of sources in our sample and determine the rough ages that correspond to our gravity classifications. Table 11 summarizes the age estimates for our sample.

4.5.1. Young Kinematic Group Members

A number of objects in our sample have been tied to young kinematic groups, which allows us to examine our gravity classifications for objects of known age. Based on their calculated index values and gravity scores, the TWA objects in our sample are all classified as VL-G, including the L3 planetary-mass companion TWA 27B (a.k.a. 2M1207b). This is in good agreement with the young age of TWA (∼8–12 Myr; Torres et al. 2008; Mentuch et al. 2008). One object in our sample, 2M 0608−27 (Rice et al. 2010b), has been recently linked to the ∼10 Myr old β Pictoris (Torres et al. 2008) moving group. 2M 0608−27 is characterized by our indices as L0 VL-G, which agrees with its possible membership in β Pictoris. Two objects in our sample, GSC 08047B (Chauvin et al. 2005a) and AB PicB (Chauvin et al. 2005b), are companions to members of the ∼30 Myr old Tuc–Hor Association. Both GSC 08047B (L1) and the AB PicB (L0) are classified as VL-G, as is 2M 0141−46 (L0 VL-G), a candidate Tuc–Hor

member (Kirkpatrick et al. 2010). Complicating the possible age for our VL-G classifications, 2M 0355+11 (L3 VL-G) has a measured space motion that is consistent with membership in the ∼100 Myr old AB Doradus moving group (Liu et al. 2013). Interestingly, CD−35 2722B, also an AB Dor member (Wahhaj et al. 2011), has only very subtle signatures of low gravity and is classified as an L3 INT-G. Figure 27 compares the spectra for these two objects. Overall, it appears that an infrared classification of VL-G corresponds to an age of ∼10–30 Myr, in agreement with the age estimate for optically classified γ objects (log(age(yr)) ≈ 7; Kirkpatrick et al. 2010). It is important to note, however, that older objects (e.g., 2M 0355+11) can also display very low gravity spectral signatures.

2M 0314+16 and 2M 1705−05 are candidate members of the ∼500 Myr old (King et al. 2003) Ursa Majoris moving group (Seifahrt et al. 2010), and neither shows signatures of low gravity. As mentioned in Section 4.3, LP 944−20 is classified as L0 FLD-G but is on the borderline for INT-G classification. LP 944−20 is thought to be a member of the ∼200 Myr old Castor moving group (Ribas 2003). Thus, though an absolute upper limit to the ages of our INT-G sources is difficult to determine from young moving group members, we appear to be sensitive to ages ≲200 Myr.

4.5.2. Objects with Lithium

A number of our sources have published lithium (Li I) detections from optical spectroscopy. The detection of lithium in the spectrum of a low-mass star or brown dwarf can imply two things: (1) the object has too little mass (≲65 M_{Jup}) to
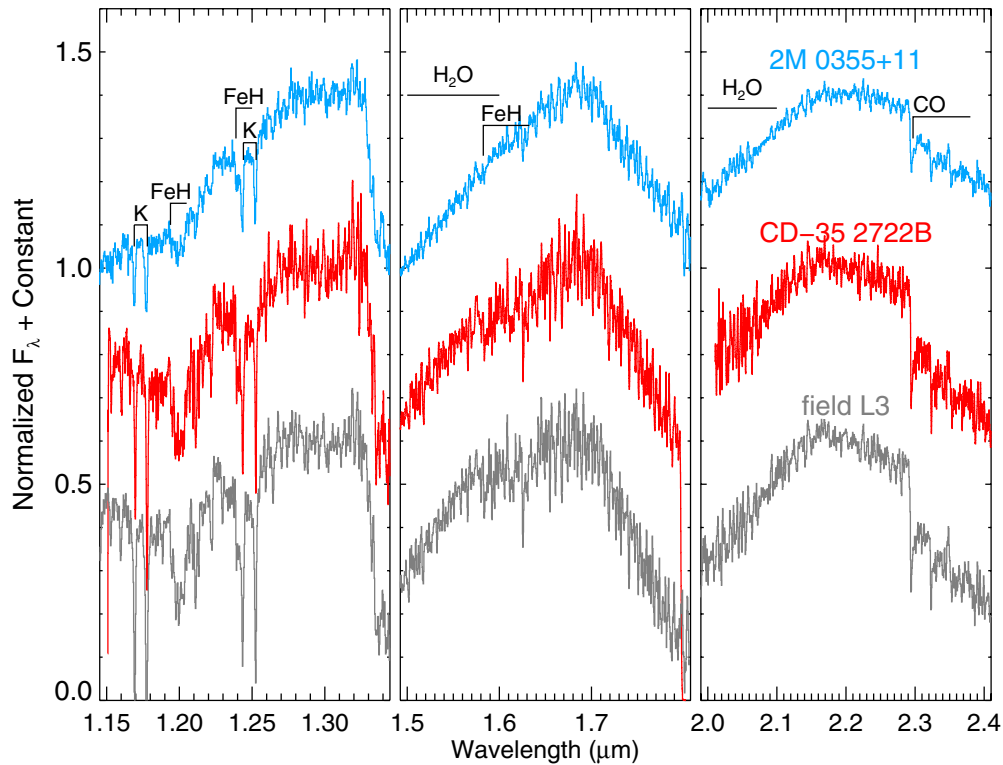
Figure 27. Moderate-resolution spectra comparing 2M 0355+11 (blue) and CD−35 2722B (red), both of which are likely members of the AB Doradus moving group (Liu et al. 2013; Wahhaj et al. 2011). A field L3 dwarf (gray; Cushing et al. 2005) is shown for comparison. The J, H, and K bands are plotted separately and normalized by the mean flux at 1.27–1.32, 1.65–1.72, and 2.15–2.25 μm, respectively. Membership in AB Dor implies that 2M 0355+11 and CD−35 2722B are the same age. Yet, based on their near-IR spectra, they are classified as having different gravities, VL-G and INT-G, respectively.

(A color version of this figure is available in the online journal.)

ever have burned lithium or (2) the object is young and has not yet depleted its lithium. For M dwarfs, a Li I detection provides a useful upper limit on the ages, with detections at later spectral types corresponding to an older upper limit on the age (Chabrier et al. 1996). For L dwarfs, however, young objects can have weaker Li I than field dwarfs (Kirkpatrick et al. 2008) due to lower surface gravity (i.e., a similar effect as seen for Na I and K I). For late L dwarfs, lithium is expected to form molecular species and Li I should not be seen in their spectra. Shkolnik et al. (2009) detected strong Li I absorption in the optical spectra of 2M 0557−13 (M7 VL-G) and 2M 0335+23 (M7 VL-G) and determined upper limits to their ages of 10 Myr, consistent with our near-IR classification. The detection of Li I in the optical spectrum of SERC 296A (M6 VL-G) has a limit on its age of $\lesssim$200 Myr (Thackrah et al. 1997), which is consistent with its classification. Both 2M 0019+46 and 2M 1411−21 are M8 INT-G objects with Li I detections (Reiners & Basri 2009), which sets an age limit for these sources of $\lesssim$300 Myr.

4.5.3. Companions to Young Stars

Six of our sources are companions to stars. Four of these objects are discussed in Section 4.5.1, as their stellar companions are known members of young kinematic groups. Two of our sources are companions to stars for which ages can be approximated. G 196−3B is classified as L3 VL-G based on its near-IR indices, and has an estimated age of 20–300 Myr (Rebolo et al. 1998; Kirkpatrick et al. 2001). The VL-G classification of G 196−3B and spectral similarity to other VL-G L3 objects (Figure 8) argue that the G 196−3 system likely falls at the low end of its estimated age range. Gl 417B is an L4.5 companion to a G0 star. We classify Gl 417B as L5 FLD-G but note that

its spectrum shows very subtle signatures of low gravity. Based on a variety of indicators, Kirkpatrick et al. (2001) estimate an age of 80–300 Myr for Gl 417B. Gyrochronology of Gl 417A, however, gives an age estimate of 750 Myr (Allers et al. 2010).

4.6. Notes on Selected Objects

4.6.1. 2MASS J22443167+2043433

With a $J - K$ color of 2.45 mag, 2M 2244+20 is one of the reddest known L dwarfs. Its optical spectrum does not show obvious signs of peculiarity (Kirkpatrick et al. 2008), but its very peculiar IR spectrum has been attributed to low gravity and/or low metallicity (McLean et al. 2003). Low metallicity seems an unlikely explanation for 2M 2244+20's peculiar spectrum, as low-metallicity objects tend to have much bluer $J - K$ colors (e.g., the sdL7 2MASS J05325346+8246465 with $J - K = 0.26$ mag; Burgasser et al. 2007). Figure 15 shows the spectrum of 2M 2244+20 (L6 VL-G) compared to 2M 0103+19, an optical L6β we classify in the infrared as an L6 INT-G, as well as the dusty L6.5 dwarf 2M 2148+40 (Looper et al. 2008). Despite its $J - K$ color being similar to 2M 2148+40 ($J - K = 2.38$ mag), the spectrum of 2M 2244+20 more closely resembles 2M 0103+29 ($J - K = 2.14$ mag). The continuum shape of 2M 2244+20's spectrum is remarkably similar to 2M 0103+29 (despite the difference in $J - K$ color for the two objects), but the K I and FeH features in 2M 2244+20 are weaker, implying that 2M 2244+20 has a lower gravity.

4.6.2. Reddened Objects

As seen in Figure 1, three of the M dwarfs in our sample (2M 0422+15, 2M 0435−14, and 2M 0619−29) have

particularly red near-IR spectra for their spectral types. We have estimated the reddening to each of these sources by comparing their 2MASS $J - K$ colors to the photospheric colors for young objects of their spectral types (Luhman et al. 2010). We find reddenings of A_v = 4.6, 7.4, and 6.5 mag for 2M 0422+15, 2M 0435−14, and 2M 0619−29, respectively. We dereddened their near-IR spectra and found that these levels of reddening do not change the spectral type or gravity determinations for these objects.

2M 0422+15 lies ∼10° south of the Taurus star-forming region in an area that has diffuse extinction of $A_v \simeq$ 0.8–1.4 mag (Lombardi et al. 2010) and CO emission (Dame et al. 2001), thus it seems plausible that it is either behind or embedded in interstellar material associated with the Taurus–Auriga region. 2M 0422+15 displays excess emission in the mid-IR (J. Lyons et al., in preparation) indicative of a circumstellar disk, which is not particularly surprising given our classification of VL-G.

The diffuse extinction measured toward 2M 0435−14 is A_v ∼1.5 mag (Schlegel et al. 1998), and no CO emission is detected in the immediate vicinity. As noted by Cruz et al. (2003), 2M 0435−14 lies in the direction of MBM20, a molecular cloud 112–161 pc away (Hearty et al. 2000). Cruz et al. (2003) calculated a spectrophotometric distance for 2M 0435−14 of 30 pc and concluded that it could not be a member of MBM20. 2M 0435−14 does not display excess emission from a disk (J. Lyons et al., in preparation) and is in front of the MBM20 cloud. Thus, the source of its reddening remains unknown.

The dust map toward 2M 0619−29 indicates very low extinction ($A_V \lesssim$ 0.2) in the region (Schlegel et al. 1998). 2M 0619−29 has mid-IR excess emission indicative of a circumstellar disk (J. Lyons et al., in preparation). With a spectral type of M5, we could not assign a gravity classification to 2M 0619−29. Qualitatively, 2M 0619−29 has low-gravity features compared to a field M5 dwarf spectrum. This, combined with the detection of a circumstellar disk for this source, makes it likely to be $\lesssim$10 Myr old, and possibly reddened by its disk.

4.6.3. 2MASS J03552337+1133437

2M 0355+11 is one of the more interesting objects in our sample. It has one of the reddest $J - K$ colors (2.52 mag) of any known L dwarf. It was classified as an L5γ by Cruz et al. (2009), and it is a mere 9.1 ± 0.1 pc away (Liu et al. 2013). Based on its kinematics and sky position, Liu et al. (2013) link 2M 0355+11 to the ∼100 Myr old AB Doradus moving group. In contrast, Faherty et al. (2013) determine that this object is unlikely to be an AB Dor member, but based on a lower precision parallax measurement. Figure 27 shows the spectrum of 2M 0355+11 compared to CD−35 2722B, a young companion to an AB Dor member (Wahhaj et al. 2011). Despite having the same infrared spectral type (L3) and nominally the same (∼100 Myr) age, the spectra of 2M 0355+11 and CD−35 2722B are quite different. The spectrum of CD−35 2722 has very subtle hints of youth, and we classify this object as INT-G, consistent with the ∼100 Myr age of AB Dor. 2M 0355+11, on the other hand, has very distinct low-gravity features, and is classified as VL-G. We note that even if 2M 0355+11 were assigned an IR spectral type of L5 (its optical spectral type), we would still classify this object as VL-G. The discrepancies between the spectra of 2M 0355+11 and CD−35 2722B are puzzling. Perhaps 2M 0355+11 and CD−35 2722 are not the same age (i.e., one of them is not a member of AB Dor)? If 2M 0355+11 and CD−35 2722 are indeed coeval,

their spectra indicate that *objects of the same age may have very different spectral signatures of youth.*

5. CONCLUSIONS

We have analyzed the largest sample to date of near-IR spectra of young ultracool dwarfs. By comparing known young objects in our sample to field dwarfs, we have found that both visual and index-based classification works well in the near-IR, producing types that are well correlated with optical spectral types. As a result, we have developed a method for determining near-IR spectral types that is gravity-insensitive.

We also have examined our spectra for gravity (age) sensitive features and have constructed a set of near-IR spectral indices that measure the depths of VO, FeH, and alkali line absorption as well as the H-band continuum shape. By comparing index measurements for young and old (field) ultracool dwarfs, we have created a scoring system and established two gravity classifications, VL-G and INT-G, for use with the near-IR spectra of M5–L6 objects. Our approach provides consistent results between optical and near-IR gravity classifications, with our VL-G and INT-G classifications corresponding to the Cruz et al. (2009) optical gravity classifications of γ and β, respectively.

A subset of our sample have ages determined by kinematically linking them to nearby young moving groups or have limits placed on their ages by the detection of Li I in their optical spectra. We estimate that objects with near-IR gravity classifications of VL-G are ∼10–30 Myr old and those with gravity classifications of INT-G are ∼50–200 Myr old, though there are exceptions to these age limits (e.g., the ≈100 Myr AB Dor member 2M 0355+11 appears to be unusually low gravity). As additional kinematic information becomes available for young field ultracool dwarfs, more can be linked to young moving groups, allowing a more detailed study of the age dependence of our classification system.

APPENDIX

EXAMPLES OF GRAVITY CLASSIFICATION

A.1. A Low-resolution Spectrum

As an example of a gravity classification for a low-resolution spectrum, we will examine the spectrum of 2MASS J17260007+1538190 (L3). Table 5 lists the calculated indices for this spectrum. We can determine the gravity scores for each of the calculated indices using the criteria listed in Table 9.

1. FeH: the FeH gravity score for low-resolution spectra is determined from the FeH_z index. The value of the FeH_z index for 2M 1726+15 is 1.220 ± 0.050. The index value is less than 1.163 (the requirement for an L3 to receive a score of 1 in this index) by more than one sigma, but does not meet the requirement to receive a score of 2 ($FeH_z \leqslant 1.357$). Thus the FeH indicator is assigned a gravity score of 1.

2. VO: the VO gravity score is determined from the VO_z index. The VO_z index of 2M 1726+15 (1.239 ± 0.035) meets the criteria to be assigned a score of 2 ($VO_z \geqslant 1.097$). Thus, the VO gravity score is 2.

3. Alkali lines: the alkali score for low-resolution spectra is determined from the K_{I_J} index. The K_{I_J} index value of 2M 1726+15 (1.111 ± 0.034) is less than 1.135 but not by more than 1σ. Thus, the alkali line gravity score for 2M 1726+15 is "?."

4. *H*-band continuum shape: the gravity score for *H*-band continuum shape is determined from the *H*-cont index. The *H*-cont index value of 2M 1726+15 (0.935 ± 0.010) meets the criteria for an L3-type object to receive a score of 1 (*H*-cont $\geqslant 0.898$) by more than 1σ. Thus 2M 1726+15 is assigned an *H*-band continuum gravity score of 1.

The median gravity score from the four indicators above (12?1) is 1, thus we assign the low-resolution spectrum of 2M 1726+15 a gravity classification of int-g.

A.2. A Moderate-resolution Spectrum

To illustrate a gravity classification for a moderate-resolution spectrum, we examine the spectrum of 2MASS J10224821+5825453 (L1). Tables 8 and 6 list the EWs and indices calculated from this spectrum. The gravity scores for VO and *H*-band continuum shape are determined in the same way as for the low-resolution spectrum example. The FeH score will include the FeH_z and FeH_J indices. The alkali line score will be determined from the EWs of the Na I and K I lines, using the criteria in Table 10.

1. FeH: the FeH gravity score for moderate-resolution spectra is determined from both the FeH_z and FeH_J indices. 2M 1022+58 has an FeH_z index (1.284 ± 0.031) that is consistent with normal field L1 dwarfs and receives a score of 0. Its FeH_J index (1.229 ± 0.024), however, meets the criteria to be scored a 1 ($FeH_J \leqslant 1.253$) by more than 1σ. Because one of the FeH indices receives a score of 1, the gravity score for FeH is 1.

2. VO: the VO gravity score is determined from the VO_z index. The VO_z index of 2M 1022+58 (1.183 ± 0.020) meets the criteria to be assigned a score of 1 ($VO_z \geqslant 1.112$) by more than 1σ. Thus, the VO gravity score is 1.

3. Alkali lines: the alkali line gravity score for moderate-resolution spectra is determined from the EWs of the *J*-band K I and Na I lines. Comparing the EWs calculated from the spectrum of 2M1022+58 (Table 8) to the criteria in Table 10, the source receives scores of 1, 0, 0, and 0 for the $1.138 \mu m$ Na I, $1.169 \mu m$ K I, $1.177 \mu m$ K I, and $1.253 \mu m$ K I line EWs, respectively. Because it did not receive a score of 1 from at least half of its line EWs, it receives an alkali line gravity score of 0.

4. *H*-band continuum shape: the gravity score for *H*-band continuum shape is determined from the *H*-cont index. The *H*-cont index value of 2M 1022+58 (0.913 ± 0.008) does not meet the criteria for an L1 to receive a score of 1, and is thus assigned an *H*-band continuum gravity score of 0.

The median gravity score from the four indicators above (1100) is 0.5. Thus, the moderate-resolution spectrum of 2M 1022+58 is assigned a gravity classification of fld-g.

REFERENCES

Allers, K. N., Jaffe, D. T., Luhman, K. L., et al. 2007, ApJ, 657, 511
Allers, K. N., Liu, M. C., Dupuy, T. J., & Cushing, M. C. 2010, ApJ, 715, 561
Allers, K. N., Liu, M. C., Shkolnik, E., et al. 2009, ApJ, 697, 824
Barman, T. S., Macintosh, B., Konopacky, Q. M., & Marois, C. 2011, ApJL, 735, L39
Boeshaar, P. C., & Tyson, J. A. 1985, AJ, 90, 817
Borysow, A., Jorgensen, U. G., & Zheng, C. 1997, A&A, 324, 185
Bowler, B. P., Liu, M. C., Dupuy, T. J., & Cushing, M. C. 2010, ApJ, 723, 850
Bowler, B. P., Liu, M. C., Shkolnik, E. L., et al. 2012, ApJ, 753, 142
Burgasser, A. J. 2007, ApJ, 659, 655
Burgasser, A. J., Cruz, K. L., Cushing, M., et al. 2010, ApJ, 710, 1142
Burgasser, A. J., Cruz, K. L., & Kirkpatrick, J. D. 2007, ApJ, 657, 494
Burgasser, A. J., Liu, M. C., Ireland, M. J., Cruz, K. L., & Dupuy, T. J. 2008, ApJ, 681, 579
Burgasser, A. J., & McElwain, M. W. 2006, AJ, 131, 1007
Burgasser, A. J., McElwain, M. W., Kirkpatrick, J. D., et al. 2004, AJ, 127, 2856
Chabrier, G., Baraffe, I., & Plez, B. 1996, ApJL, 459, L91
Chauvin, G., Lagrange, A.-M., Dumas, C., et al. 2004, A&A, 425, L29
Chauvin, G., Lagrange, A.-M., Lacombe, F., et al. 2005a, A&A, 430, 1027
Chauvin, G., Lagrange, A.-M., Zuckerman, B., et al. 2005b, A&A, 438, L29
Chiu, K., Fan, X., Leggett, S. K., et al. 2006, AJ, 131, 2722
Covey, K. R., Lada, C. J., Román-Zúñiga, C., et al. 2010, ApJ, 722, 971
Cruz, K. L., Burgasser, A. J., Reid, I. N., & Liebert, J. 2004, ApJL, 604, L61
Cruz, K. L., Kirkpatrick, J. D., & Burgasser, A. J. 2009, AJ, 137, 3345
Cruz, K. L., Reid, I. N., Kirkpatrick, J. D., et al. 2007, AJ, 133, 439
Cruz, K. L., Reid, I. N., Liebert, J., Kirkpatrick, J. D., & Lowrance, P. J. 2003, AJ, 126, 2421
Cushing, M. C., Rayner, J. T., & Vacca, W. D. 2005, ApJ, 623, 1115
Cushing, M. C., Tokunaga, A. T., & Kobayashi, N. 2000, AJ, 119, 3019
Cushing, M. C., Vacca, W. D., & Rayner, J. T. 2004, PASP, 116, 362
Dame, T. M., Hartmann, D., & Thaddeus, P. 2001, ApJ, 547, 792
Faherty, J. K., Burgasser, A. J., Cruz, K. L., et al. 2009, AJ, 137, 1
Faherty, J. K., Burgasser, A. J., Walter, F. M., et al. 2012, ApJ, 752, 56
Faherty, J. K., Rice, E. L., Cruz, K. L., Mamajek, E. E., & Núñez, A. 2013, AJ, 145, 2
Geballe, T. R., Knapp, G. R., Leggett, S. K., et al. 2002, ApJ, 564, 466
Geißler, K., Metchev, S., Kirkpatrick, J. D., Berriman, G. B., & Looper, D. 2011, ApJ, 732, 56
Gizis, J. E. 2002, ApJ, 575, 484
Gizis, J. E., Faherty, J. K., Liu, M. C., et al. 2012, AJ, 144, 94
Gorlova, N. I., Meyer, M. R., Rieke, G. H., & Liebert, J. 2003, ApJ, 593, 1074
Hawley, S. L., Covey, K. R., Knapp, G. R., et al. 2002, AJ, 123, 3409
Hearty, T., Fernández, M., Alcalá, J. M., Covino, E., & Neuhäuser, R. 2000, A&A, 357, 681
Joyce, R. R., Hinkle, K. H., Wallace, L., Dulick, M., & Lambert, D. L. 1998, AJ, 116, 2520
Kastner, J. H., Zuckerman, B., & Bessell, M. 2008, A&A, 491, 829
King, J. R., Villarreal, A. R., Soderblom, D. R., Gulliver, A. F., & Adelman, S. J. 2003, AJ, 125, 1980
Kirkpatrick, J. D. 2005, ARA&A, 43, 195
Kirkpatrick, J. D., Barman, T. S., Burgasser, A. J., et al. 2006, ApJ, 639, 1120
Kirkpatrick, J. D., Cruz, K. L., Barman, T. S., et al. 2008, ApJ, 689, 1295
Kirkpatrick, J. D., Dahn, C. C., Monet, D. G., et al. 2001, AJ, 121, 3235
Kirkpatrick, J. D., Henry, T. J., & Simons, D. A. 1995, AJ, 109, 797
Kirkpatrick, J. D., Looper, D. L., Burgasser, A. J., et al. 2010, ApJS, 190, 100
Kirkpatrick, J. D., Reid, I. N., Liebert, J., et al. 1999, ApJ, 519, 802
Kirkpatrick, J. D., Reid, I. N., Liebert, J., et al. 2000, AJ, 120, 447
Kleinmann, S. G., & Hall, D. N. B. 1986, ApJS, 62, 501
Knapp, G. R., Leggett, S. K., Fan, X., et al. 2004, AJ, 127, 3553
Lagrange, A.-M., Kasper, M., Boccaletti, A., et al. 2009, A&A, 506, 927
Liu, M. C., Dupuy, T. J., & Allers, K. N. 2013, AN, 334, 85
Lodieu, N., Hambly, N. C., Jameson, R. F., & Hodgkin, S. T. 2008, MNRAS, 383, 1385
Lombardi, M., Lada, C. J., & Alves, J. 2010, A&A, 512, A67
Looper, D. L., Burgasser, A. J., Kirkpatrick, J. D., & Swift, B. J. 2007, ApJL, 669, L97
Looper, D. L., Kirkpatrick, J. D., Cutri, R. M., et al. 2008, ApJ, 686, 528
Lovis, C., & Mayor, M. 2007, A&A, 472, 657
Lucas, P. W., Roche, P. F., Allard, F., & Hauschildt, P. H. 2001, MNRAS, 326, 695

Luhman, K. L., Adame, L., D'Alessio, P., et al. 2005, ApJL, 635, L93
Luhman, K. L., Allen, P. R., Espaillat, C., Hartmann, L., & Calvet, N. 2010, ApJS, 186, 111
Madhusudhan, N., Burrows, A., & Currie, T. 2011, ApJ, 737, 34
Marois, C., Macintosh, B., Barman, T., et al. 2008, Sci, 322, 1348
Martín, E. L., Basri, G., & Zapatero Osorio, M. R. 1999a, AJ, 118, 1005
Martín, E. L., Delfosse, X., Basri, G., et al. 1999b, AJ, 118, 2466
Martín, E. L., Phan-Bao, N., Bessell, M., et al. 2010, A&A, 517, A53
McGovern, M. R., Kirkpatrick, J. D., McLean, I. S., et al. 2004, ApJ, 600, 1020
McLean, I. S., McGovern, M. R., Burgasser, A. J., et al. 2003, ApJ, 596, 561
Mentuch, E., Brandeker, A., van Kerkwijk, M. H., Jayawardhana, R., & Hauschildt, P. H. 2008, ApJ, 689, 1127
Metchev, S. A., Kirkpatrick, J. D., Berriman, G. B., & Looper, D. 2008, ApJ, 676, 1281
Meyer, M. R., Edwards, S., Hinkle, K. H., & Strom, S. E. 1998, ApJ, 508, 397
Morgan, W. W., Keenan, P. C., & Kellman, E. 1943, An Atlas of Stellar Spectra, with an Outline of Spectral Classification (Chicago, IL: Univ. Chicago Press)
Patience, J., King, R. R., De Rosa, R. J., et al. 2012, A&A, 540, A85
Rayner, J. T., Toomey, D. W., Onaka, P. M., et al. 2003, PASP, 115, 362
Rebolo, R., Zapatero Osorio, M. R., Madruga, S., et al. 1998, Sci, 282, 1309
Reid, I. N., Burgasser, A. J., Cruz, K. L., Kirkpatrick, J. D., & Gizis, J. E. 2001, AJ, 121, 1710
Reid, I. N., Cruz, K. L., Kirkpatrick, J. D., et al. 2008, AJ, 136, 1290
Reid, I. N., Kirkpatrick, J. D., Liebert, J., et al. 2002, AJ, 124, 519
Reiners, A., & Basri, G. 2009, ApJ, 705, 1416
Ribas, I. 2003, A&A, 400, 297
Rice, E. L., Barman, T., Mclean, I. S., Prato, L., & Kirkpatrick, J. D. 2010a, ApJS, 186, 63
Rice, E. L., Faherty, J. K., & Cruz, K. L. 2010b, ApJL, 715, L165
Salim, S., Lépine, S., Rich, R. M., & Shara, M. M. 2003, ApJL, 586, L149

Schlegel, D. J., Finkbeiner, D. P., & Davis, M. 1998, ApJ, 500, 525
Schmidt, S. J., Cruz, K. L., Bongiorno, B. J., Liebert, J., & Reid, I. N. 2007, AJ, 133, 2258
Scholz, A., Muzic, K., Geers, V., et al. 2012, ApJ, 744, 6
Scholz, R.-D., McCaughrean, M. J., Zinnecker, H., & Lodieu, N. 2005, A&A, 430, L49
Seifahrt, A., Reiners, A., Almaghrbi, K. A. M., & Basri, G. 2010, A&A, 512, A37
Shkolnik, E., Liu, M. C., & Reid, I. N. 2009, ApJ, 699, 649
Shkolnik, E. L., Anglada-Escude, G., Liu, M. C., et al. 2012, ApJ, 758, 56
Slesnick, C. L., Hillenbrand, L. A., & Carpenter, J. M. 2004, ApJ, 610, 1045
Spiegel, D. S., Burrows, A., & Milsom, J. A. 2011, ApJ, 727, 57
Stauffer, J. R., Schultz, G., & Kirkpatrick, J. D. 1998, ApJL, 499, L199
Stephens, D. C., Leggett, S. K., Cushing, M. C., et al. 2009, ApJ, 702, 154
Testi, L., D'Antona, F., Ghinassi, F., et al. 2001, ApJL, 552, L147
Thackrah, A., Jones, H., & Hawkins, M. 1997, MNRAS, 284, 507
Tinney, C. G., & Reid, I. N. 1998, MNRAS, 301, 1031
Tokunaga, A. T., & Kobayashi, N. 1999, AJ, 117, 1010
Torres, C. A. O., Quast, G. R., Melo, C. H. F., & Sterzik, M. F. 2008, in Handbook of Star Forming Regions, Volume II, The Southern Sky, ed. B. Reipurth (San Francisco: ASP), 757
Torres, G., Guenther, E. W., Marschall, L. A., et al. 2003, AJ, 125, 825
Vacca, W. D., Cushing, M. C., & Rayner, J. T. 2003, PASP, 115, 389
Wahhaj, Z., Liu, M. C., Biller, B. A., et al. 2011, ApJ, 729, 139
Webb, R. A., Zuckerman, B., Platais, I., et al. 1999, ApJL, 512, L63
Weights, D. J., Lucas, P. W., Roche, P. F., Pinfield, D. J., & Riddick, F. 2009, MNRAS, 392, 817
Weinberger, A. J., Anglada-Escudé, G., & Boss, A. P. 2013, ApJ, 762, 118
West, A. A., Hawley, S. L., Bochanski, J. J., et al. 2008, AJ, 135, 785
West, A. A., Morgan, D. P., Bochanski, J. J., et al. 2011, AJ, 141, 97